

# Evolution of the crystal structure and magnetic properties of $\text{Sr}_{2-x}\text{Ca}_x\text{CrSbO}_6$ with composition

Emily C. Hunter and Peter D. Battle\*

Inorganic Chemistry Laboratory, University of Oxford, South Parks Road, Oxford, OX1 3QR, U. K.

\* author to whom correspondence should be addressed: [peter.battle@chem.ox.ac.uk](mailto:peter.battle@chem.ox.ac.uk)

## Abstract

Polycrystalline samples of compositions in the perovskite solid solution  $\text{Sr}_{2-x}\text{Ca}_x\text{CrSbO}_6$  ( $x=0, 0.25, 0.5, 0.75, 1.0, 1.25, 1.50, 1.75, 2.0$ ) were synthesized and characterised by synchrotron x-ray diffraction and SQUID magnetometry. Neutron powder diffraction data were collected on the  $x=0, 0.25, 0.5, 1.0, 1.5$  and  $2.0$  compositions. It was found that  $\text{Sr}_2\text{CrSbO}_6$  crystallised in the triclinic  $\bar{1}\bar{1}$  space group. The other compositions were all found to crystallise in the monoclinic space group  $P2_1/n$  although  $\text{Sr}_{1.5}\text{Ca}_{0.5}\text{CrSbO}_6$  was found to be phase separated into a calcium-deficient and calcium-rich phase, both having the space group  $P2_1/n$ .  $\text{Sr}_2\text{CrSbO}_6$  was found to order antiferromagnetically at 12 K and the ordered  $\text{Cr}^{3+}$  moment was refined to be  $2.39(1) \mu_B$ . The antiferromagnetic order was rapidly quenched on doping with Ca and compositions with  $x \geq 0.75$  exhibited ferromagnetic order.  $T_C$  increased with  $x$  to reach a maximum of 14 K at  $x=2.0$ , with an ordered moment of  $2.56(3) \mu_B$  per  $\text{Cr}^{3+}$  cation. The tilt angles of the B-site octahedra about  $[110]$  and  $[001]$  increase from  $5.4(1)^\circ$  and  $4.6(1)^\circ$  to  $13.7(1)^\circ$  and  $13.9(1)^\circ$ , respectively, across the series; the switch from antiferromagnetism to ferromagnetism occurs when both tilts are at a value of  $\sim 8^\circ$ .

## Introduction

Double perovskites have the general formula  $A_2BB'\text{O}_6$  where  $A$  is normally a divalent alkaline-earth or trivalent rare-earth cation,  $B$  is a transition-metal cation and  $B'$  is either a second transition metal or a  $p$ -block metal. The structure consists of corner sharing  $\text{BO}_6$  and  $B'\text{O}_6$  octahedra with the  $A$  cations filling the voids between the octahedra. If the cations  $B$  and  $B'$  vary significantly in size and/or charge, then cation ordering can occur so that  $\text{BO}_6$  and  $B'\text{O}_6$  octahedra alternate to give a 3D checkerboard arrangement. Double perovskites have been shown to exhibit a range of properties from colossal magnetoresistance in  $\text{Sr}_2\text{FeMoO}_6$ <sup>1</sup> to multiferroic behaviour in  $\text{La}_2\text{CoMnO}_6$ <sup>2</sup> and they are thus of interest from a technological, as well as a fundamental, point of view.

In 2007 two new double perovskites,  $\text{Sr}_2\text{CrSbO}_6$  and  $\text{Ca}_2\text{CrSbO}_6$ , were synthesised and characterised<sup>3</sup>. Both compounds show a high degree of B-site ordering; 93 % in  $\text{Sr}_2\text{CrSbO}_6$  and 97 % in  $\text{Ca}_2\text{CrSbO}_6$ . This pair of compounds is particularly interesting because simply changing the diamagnetic A-site cation alters the nature of the long-range magnetic order seen at low temperatures from antiferromagnetic to ferromagnetic and, furthermore,  $\text{Ca}_2\text{CrSbO}_6$  was the first example of a ferromagnetic double perovskite containing a non-magnetic  $p$  block ion on the  $B'$  site and non-magnetic ions on the A site. Retuerto *et al*

hypothesised that the composition dependence of the magnetic behaviour arose from there being a greater degree of octahedral tilting in  $\text{Ca}_2\text{CrSbO}_6$  than in  $\text{Sr}_2\text{CrSbO}_6$ <sup>3</sup>. However, this explanation has never been thoroughly tested. We have therefore made several compositions in the solid solution  $\text{Sr}_{2-x}\text{Ca}_x\text{CrSbO}_6$  in order to determine how the degree of tilting varies with composition. In the case of  $\text{Sr}_2\text{CrSbO}_6$  we have also addressed the inconsistencies in space-group assignment that exist between earlier studies<sup>3, 4</sup> and produced a model that does not involve an anomalous value for the ordered magnetic moment<sup>3</sup> in the antiferromagnetic phase.

## Experimental

Polycrystalline samples of the solid solution  $\text{Sr}_{2-x}\text{Ca}_x\text{CrSbO}_6$  ( $x=0, 0.25, 0.5, 0.75, 1.0, 1.25, 1.50, 1.75, 2.0$ ) were synthesised using the traditional ceramic method. Stoichiometric quantities of  $\text{SrCO}_3$ ,  $\text{Cr}_2\text{O}_3$  and  $\text{Sb}_2\text{O}_3$  (except for  $x=0$  where  $\text{Sb}_2\text{O}_5$  was used instead) were mixed and ground together for 30 minutes in an agate pestle and mortar and were then fired at 1100 °C for 16 hours as a loose powder. The reaction mixture was then pelletised and heated at 1150 °C for 6 hours, reground, and fired at 1150 °C for a further 24 hours. It was then fired twice at 1250 °C for 48 hours at a time. After each firing the sample was quenched to room temperature and re-ground and re-pelletized. The progress of the reaction was monitored by powder x-ray diffraction and the reaction was deemed complete when there was no further change in the x-ray powder diffraction pattern. The colour of the samples across the series evolved from deep pink for  $x=0$  to dark brown for  $x=2$ .

X-ray powder diffraction data were collected in our laboratory on a PAN'alytical Empyrean diffractometer operating with Cu  $K_{\alpha 1}$  radiation over an angular range of  $5 \leq 2\theta/^\circ \leq 125$  at room temperature. Further powder diffraction data were collected with a wavelength  $\lambda=0.8259$  Å on instrument I11 at the RAL Diamond Light Source. In the latter case, the samples were loaded into a 0.3 mm diameter borosilicate glass capillary and data were collected at room temperature by conducting a 30 minute constant-velocity scan over an angular range of  $0 \leq 2\theta/^\circ \leq 150$  using a Multi-Analyser-Crystal (MAC) detector. A silicon standard was used to determine the wavelength. The data were analysed using the Rietveld method<sup>5</sup>, as implemented in the GSAS program suite<sup>6</sup>, in order to determine the unit cell parameters. A cylindrical absorption correction for each sample was estimated using the Argonne X-ray Absorption calculator<sup>7</sup>. A pseudo-Voigt function<sup>8</sup> was employed to model the peak shapes and the background was modelled using a 20-term shifted Chebyshev function.

Neutron powder diffraction (NPD) data were collected at selected temperatures using the instruments D1b and D2b at the ILL, Grenoble. For the compositions  $x=0, 0.25, 0.5, 1.0, 1.5$  and 2 data were collected on D1b in 1 K temperature steps over the temperature range  $2 \leq T/K \leq 20$  with an angular range of  $0 \leq 2\theta/^\circ \leq 130$  using a neutron wavelength of 2.52 Å. The samples were loaded into a 6 mm diameter vanadium canister and mounted in a standard ILL orange cryostat. In the case of the  $x=0, 0.5$  and 1.0 compositions additional high-resolution NPD data were collected on D2b at 2 K, 25 K and 300 K over the angular range  $0 \leq 2\theta/^\circ \leq 160$  in steps of  $\Delta 2\theta = 0.05^\circ$  using a wavelength of 1.594 Å. All samples were mounted in a cryofurnace for data collections below room temperature. The  $x=0$  sample was also mounted in a cryofurnace during data collection at 300 K but the  $x=0.5$  and  $x=1$  samples were not. Patterns collected in the cryofurnace contained additional peaks arising from the sample environment, which were excluded from the refinements. All data were fully analysed using the Rietveld method. A pseudo-Voigt function<sup>8</sup> was employed to model the peak shapes and the background was modelled using a 12-term shifted Chebyshev function.

Dc magnetometry data were collected on a Quantum Design SQUID magnetometer. The measurements were taken on warming the sample through the temperature range  $2 \leq T/K \leq 300$  in a field of 100 Oe, firstly after cooling from room temperature to 2 K in zero field (ZFC) and subsequently after cooling in the measuring field (FC). The magnetisation per formula unit (f. u.) of the sample was also measured as a function of applied field at 2.5 K over a field range of  $-50 \leq H/\text{kOe} \leq 50$ .

## Results

### **Sr<sub>2</sub>CrSbO<sub>6</sub>**

The space groups  $I2/m$  and  $P2_1/n$  have been previously suggested for Sr<sub>2</sub>CrSbO<sub>6</sub><sup>3, 4</sup> and our x-ray diffraction data initially appeared to be consistent with the  $I2/m$  model. However the symmetry needed to be lowered to  $\bar{I}\bar{1}$  to account for all of the peak splitting observed in the high-resolution NPD data. Refinements in this space group gave lattice parameters at 300 K of  $a=5.55664(8)$  Å,  $b=5.57821(8)$  Å,  $c=7.84771(10)$  Å,  $\alpha=89.9979(32)^\circ$ ,  $\beta=89.9668(24)^\circ$  and  $\gamma=89.9374(11)^\circ$ . The fit to the data collected at 300 K is shown in Figure 1a. The absence of (ooe) and (eeo) reflections<sup>4, 9</sup> in both the x-ray and neutron diffraction data in combination with the significant distortion of the unit cell led us to conclude that the  $\bar{I}\bar{1}$  model was more appropriate than those based on either  $P2_1/n$  or  $I2/m$ . Reanalysing the synchrotron x-ray diffraction data in the space group  $\bar{I}\bar{1}$  improved the fit, with  $\chi^2$  decreasing from 11.89 to

9.539 and  $R_{wp}$  decreasing from 0.1481 to 0.1328. From the synchrotron x-ray data the B sites were found to be almost completely ordered with the 2f site being 97.9(1) % occupied by  $Cr^{3+}$ . The B site occupancies determined by neutron diffraction were within error of the values refined from the synchrotron data and, as the error was smaller in the synchrotron data, the occupancy of the B sites in the neutron refinement was fixed at the value derived from the synchrotron data in all subsequent analyses of data collected on this composition. Full details of all the structural parameters of  $Sr_2CrSbO_6$  derived from the neutron refinements can be found in Tables 1, 2 and 3.

The temperature dependence of the zero field cooled (ZFC) and field cooled (FC) magnetic susceptibilities of  $Sr_2CrSbO_6$  are shown in Figure 2. As previously reported<sup>3</sup>,  $Sr_2CrSbO_6$  behaves a paramagnet until it orders antiferromagnetically on cooling below 12 K. Below 5 K there appears to be a paramagnetic tail. The previous magnetometry study on  $Sr_2CrSbO_6$  only considered the region  $T \geq 5$  K and this feature was therefore not observed. The inverse susceptibility follows the Curie-Weiss law above  $T_N$ . A Curie-Weiss fit over the temperature range  $50 \leq T/K \leq 300$  yielded a Weiss temperature,  $\theta_W$ , of -12.23(15) K and an effective magnetic moment per  $Cr^{3+}$  cation of 3.705(6)  $\mu_B$ .

The data collected on D2b at 2 K were also refined in the space group  $\bar{I}\bar{1}$  and the distortion away from monoclinic symmetry was found to be more pronounced, with the refinement yielding lattice parameters of  $a=5.53808(22)$  Å,  $b=5.53662(23)$  Å,  $c=7.89660(14)$  Å,  $\alpha=90.1931(27)^\circ$ ,  $\beta=89.8548(30)^\circ$  and  $\gamma=90.0665(13)^\circ$ , see Figure 1b. When allowed to refine freely, the  $U_{iso}$  values on the 2f and 2g sites became negative but within one standard deviation of zero and so their value was fixed to zero in all subsequent refinements. The data at 2 K contained additional peaks at low angle, consistent with the presence of Type I magnetic ordering<sup>10</sup>. Thus the structural parameters at 2 K reported in Tables 1,2 and 3 were obtained from a refinement of the D2b data that included a Type I magnetically-ordered phase. The structural model refined from the D2b NPD data collected at 2 K was used to model the D1b data, see Figure 3; the wavelength was refined with the lattice parameters fixed at the values determined using D2b. The nuclear structure was also held fixed and only the magnetic structure was refined. It was found to be similar to that published previously, see Figure 4, but with  $m_{x1}=-m_{x2}$ ;  $m_y=0$  and  $m_{z1}=-m_{z2}$ , rather than  $m_{y1}=m_{y2}$ . This alteration, as well as the change in the space group from  $P2_1/n$  to  $\bar{I}\bar{1}$ , gave a refined ordered  $Cr^{3+}$  moment,  $M_O$ , of 2.39(1)  $\mu_B$ , somewhat higher than the previously reported value of 1.64  $\mu_B$ <sup>3</sup>. The refined ordered moment decreases on warming the sample, as shown in Figure 5, and the

magnetic Bragg reflections are not apparent above 12 K, in agreement with the SQUID magnetometry data. The fit to the data collected in the paramagnetic phase at 25 K on D2b is shown in Figure S1.

### **Crystal structure of $\text{Sr}_{1.75}\text{Ca}_{0.25}\text{CrSbO}_6$ ( $x = 0.25$ )**

Although not clearly visible in the synchrotron x-ray diffraction (SXRd) data, weak reflections indicating the presence of an (ooe) tilt<sup>4, 9</sup> were evident in the NPD data collected on D1b for  $\text{Sr}_{1.75}\text{Ca}_{0.25}\text{CrSbO}_6$ , suggesting that the space group is  $P2_1/n$ . Refinement of the SXRd data in this space group yielded lattice parameters of  $a=5.565817(6)$  Å,  $b=5.543283(7)$  Å,  $c=7.831500(9)$  Å and  $\beta=90.0031(5)^\circ$  with  $\chi^2=3.501$  and  $R_{\text{wp}}=0.0916$ . These refinements revealed that  $\text{Sr}_{1.75}\text{Ca}_{0.25}\text{CrSbO}_6$  contains an impurity phase with the same structure as  $\text{Sr}_2\text{Sb}_2\text{O}_7$  and  $\text{Ca}_2\text{Sb}_2\text{O}_7$  and with lattice parameters,  $a=7.36095(32)$  Å,  $b=10.3065(5)$  Å and  $c=7.53722(34)$  Å, that lie between those of these two compounds<sup>11, 12</sup>. We assumed that the lattice parameters of the solid-solution  $\text{Sr}_{2-x}\text{Ca}_x\text{Sb}_2\text{O}_7$  would follow Vegard's law and thus estimated the composition of the impurity phase as  $\text{Sr}_{0.84}\text{Ca}_{1.16}\text{Sb}_2\text{O}_7$ . With this composition the concentration of the impurity phase was found to be 0.91 mol %. The composition of  $\text{Sr}_{1.75}\text{Ca}_{0.25}\text{CrSbO}_6$  was adjusted to  $\text{Sr}_{1.76}\text{Ca}_{0.24}\text{Cr}_{1.01}\text{Sb}_{0.99}\text{O}_6$  in a further refinement to compensate for the impurity phase. The structural information derived from the synchrotron data collected at room temperature after this final refinement is listed in Tables S1, S3 and S5.

### **Crystal structure of $\text{Sr}_{1.5}\text{Ca}_{0.5}\text{CrSbO}_6$ ( $x = 0.5$ )**

The structure of  $\text{Sr}_{1.5}\text{Ca}_{0.5}\text{CrSbO}_6$  is more complex. It was found that the space group  $P2_1/n$  could not provide an adequate fit to either the NPD or the SXRd data, particularly at high scattering angles. Lowering the symmetry to  $P\bar{1}$  still did not account for all the peak splitting. Trying to fit the data using a 2-phase model that assumed the sample was a mixture of the end-member  $I\bar{1}$  phase and the  $P2_1/n$  phase resulted in a worse fit. However, using a 2-phase model wherein both phases adopted  $P2_1/n$  symmetry improved the fit considerably in comparison to the single-phase  $P\bar{1}$  model, with  $\chi^2$  dropping from 6.632 to 3.935 and  $R_{\text{wp}}$  from 0.0529 to 0.0407, see Figure 6. The lattice parameters of these two phases were refined to be  $a=5.54989(8)$  Å,  $b=5.53228(10)$  Å,  $c=7.84771(10)$  Å,  $\beta=90.022(6)^\circ$  and  $a=5.53317(24)$  Å,  $b=5.52279(20)$  Å,  $c=7.80851(25)$  Å,  $\beta=90.054(6)^\circ$  at 300 K. Full Rietveld fits to the NPD data collected at 300 K, 25 K and 2 K using the 2-phase model are shown in Figures S2-S4. A  $\text{Sr}_{2-x}\text{Ca}_x\text{Sb}_2\text{O}_7$  impurity phase was also found to be present in  $\text{Sr}_{1.5}\text{Ca}_{0.5}\text{CrSbO}_6$  and using the

same strategy as before the sample was found to contain 1.81 mol %  $\text{Sr}_{0.61}\text{Ca}_{1.39}\text{Sb}_2\text{O}_7$ . The Cr:Sb ratio of  $\text{Sr}_{1.5}\text{Ca}_{0.5}\text{CrSbO}_6$  was adjusted to 1.02:0.98 to compensate for the impurity phase. Given that a plot of unit cell volume,  $V$ , against  $x$  for  $\text{Sr}_{2-x}\text{Ca}_x\text{CrSbO}_6$  is approximately linear (see Figure 9) the compositions of the two  $P2_1/n$  phases of nominal  $\text{Sr}_{1.5}\text{Ca}_{0.5}\text{CrSbO}_6$  were estimated using Vegard's law to be  $\text{Sr}_{1.55}\text{Ca}_{0.45}\text{Cr}_{1.02}\text{Sb}_{0.98}\text{O}_6$  and  $\text{Sr}_{1.33}\text{Ca}_{0.67}\text{Cr}_{1.02}\text{Sb}_{0.98}\text{O}_6$ . Our two-phase refinements then found the perovskite to be composed of 65 mol % of the Sr-rich phase and 35 mol % of the Ca-rich phase, giving an overall composition of  $\text{Sr}_{1.47}\text{Ca}_{0.53}\text{Cr}_{1.02}\text{Sb}_{0.98}\text{O}_6$ , which is consistent with the stoichiometry synthesized. Full details of all the structural parameters of  $\text{Sr}_{1.55}\text{Ca}_{0.45}\text{Cr}_{1.02}\text{Sb}_{0.98}\text{O}_6$  and  $\text{Sr}_{1.33}\text{Ca}_{0.67}\text{Cr}_{1.02}\text{Sb}_{0.98}\text{O}_6$  refined from the NPD data are listed in Tables 4 - 7.

### **Magnetic properties of $\text{Sr}_{1.75}\text{Ca}_{0.25}\text{CrSbO}_6$ ( $x = 0.25$ ) and $\text{Sr}_{1.5}\text{Ca}_{0.5}\text{CrSbO}_6$ ( $x = 0.5$ )**

As shown in Figures 7, both  $\text{Sr}_{1.75}\text{Ca}_{0.25}\text{CrSbO}_6$  and nominal  $\text{Sr}_{1.5}\text{Ca}_{0.5}\text{CrSbO}_6$  appear to be paramagnetic down to 2 K and to obey the Curie-Weiss law to low temperatures. A Curie-Weiss fit over the region  $50 \leq T/\text{K} \leq 300$  yielded a Weiss temperature,  $\theta_W$ , of -7.17(19) K and an effective magnetic moment per  $\text{Cr}^{3+}$  cation,  $\mu_{\text{eff}(\text{Cr})}$ , of 3.841(8)  $\mu_B$  for  $\text{Sr}_{1.75}\text{Ca}_{0.25}\text{CrSbO}_6$  and  $\theta_W = -0.4(3)$  K and  $\mu_{\text{eff}(\text{Cr})} = 3.657(12)$   $\mu_B$  for  $\text{Sr}_{1.5}\text{Ca}_{0.5}\text{CrSbO}_6$ . However, small magnetic Bragg peaks consistent with the magnetic structure of  $\text{Sr}_2\text{CrSbO}_6$  were visible in the D1b data collected below 5 K for  $\text{Sr}_{1.75}\text{Ca}_{0.25}\text{CrSbO}_6$  (see Figure 8a); the same peaks are visible at 2 K in the case of  $\text{Sr}_{1.50}\text{Ca}_{0.50}\text{CrSbO}_6$  (see Figure 8b) and can be fitted using the same magnetic structure as  $\text{Sr}_2\text{CrSbO}_6$  to give an ordered Cr(III) moment,  $M_O$ , at 2 K of 1.79(3)  $\mu_B$  for  $\text{Sr}_{1.75}\text{Ca}_{0.25}\text{CrSbO}_6$  and 0.76(5)  $\mu_B$  for  $\text{Sr}_{1.5}\text{Ca}_{0.5}\text{CrSbO}_6$ . The latter composition contains two perovskite phases and the antiferromagnetic phase giving rise to the ordered moment was assumed to be associated with the more Sr-rich  $x=0.45$  phase; no magnetic contribution from the Ca-rich phase was included in the refinement. If the second phase had also been treated as antiferromagnetic the ordered moment per  $\text{Cr}^{3+}$  cation would have been reduced proportionately. However, our assumption that a paramagnetic phase is present is consistent with the absence of a maximum in  $\chi(T)$  at 5 K

### **$\text{Sr}_{2-x}\text{Ca}_x\text{CrSbO}_6$ ( $x=0.75, 1, 1.25, 1.50, 1.75, 2.0$ )**

Samples of these compositions contained only one perovskite phase. The evolution of the lattice parameters across the whole  $\text{Sr}_{2-x}\text{Ca}_x\text{CrSbO}_6$  series is shown in Figure 9. Analysis of our X-ray and neutron data showed that all of the compounds in the composition range  $0.75 \leq x \leq 2.0$  adopt the space group  $P2_1/n$ . The  $a$  and  $b$  lattice parameters are within error of

each other for  $x=0.75$  and  $x=1.0$  after which they start to diverge with  $b$  remaining almost constant and  $a$  decreasing. The  $c$  lattice parameter decreases approximately linearly across the series. Given the closeness of  $a$  and  $b$  for  $x=0.75$  and  $x=1.0$ , tetragonal space groups were considered but none could provide a comparable fit to  $P2_1/n$ . Given that  $\text{Sr}_2\text{CrSbO}_6$  adopts a triclinic structure, all compositions were also modelled in  $P\bar{1}$  but this did not significantly improve the fit achieved in  $P2_1/n$ . High resolution NPD data were collected at 300 K on  $\text{SrCaCrSbO}_6$  from which the lattice parameters were refined to be  $a=5.50868(8)$ ,  $b=5.50863(7)$ ,  $c=7.78357(6)$  and  $\beta=89.9649(17)^\circ$ . The statistically significant deviation of  $\beta$  from  $90^\circ$  justifies the monoclinic symmetry used for this compound despite the closeness of  $a$  and  $b$ . The  $\text{Sr}_{1-x}\text{Ca}_x\text{Sb}_2\text{O}_7$  impurity was present in all compounds in the series; the concentration decreased with increasing Ca content. In each case the composition of the impurity was calculated using Vegard's law and the composition of the perovskite phase was adjusted accordingly.  $\text{SrCaCrSbO}_6$  contained the largest amount of impurity at 4.16 mol % with all other phases containing less than 2.6 mol %  $\text{Sr}_{1-x}\text{Ca}_x\text{Sb}_2\text{O}_7$ . The percentage and composition of  $\text{Sr}_{1-x}\text{Ca}_x\text{Sb}_2\text{O}_7$  in each phase, as well as the adjusted composition of the perovskite phase can be found in Table S7. We note that the sample used in the previous study of  $\text{Ca}_2\text{CrSbO}_6$  also contained a similar concentration of the  $\text{Ca}_2\text{Sb}_2\text{O}_7$  impurity as can be seen from the XRD pattern shown in their Figure 1b<sup>3</sup>. Rietveld fits of NPD patterns of  $\text{SrCaCrSbO}_6$  collected at 300 K, 25 K and 2 K are shown in Figures S5-S7. The structural information deduced from the neutron refinements can be found in Tables 8, 9 and 10 and the structural information deduced from the SXRD data for the other compositions can be found in Tables S1-S6.

As shown by the temperature dependence of the susceptibility, see Figure 10, all of the compositions in the composition range  $0.75 \leq x \leq 2.0$  are ferromagnetic with  $T_C$  increasing from 3.5 K for  $\text{Sr}_{1.25}\text{Ca}_{0.75}\text{CrSbO}_6$  to 14 K for  $\text{Ca}_2\text{CrSbO}_6$ . The Weiss temperature extracted from the Curie-Weiss fit to the paramagnetic regime of each compound, see Table 11, becomes increasingly positive as  $x$  increases showing that the net magnetic interactions are increasingly ferromagnetic, as expected. These data suggest, see Figure 11, that the magnetic interactions are dominated by ferromagnetic exchange in compositions with  $x > 0.5$ . The Weiss temperature reaches a plateau for  $x > 1.75$ , suggesting that a limit in the strength of the ferromagnetic interactions has been reached.  $M(H)$  curves collected at 2.5 K, see Figure 12, confirm that all six compounds in this composition range are ferromagnetic and that the saturation magnetisations,  $M_S$ , of the  $x=1.75$  and  $x=2.00$  compounds are similar at  $2.64 \mu_B$



and  $2.60 \mu_B$  per formula unit, respectively. For compositions where  $x < 1.75$  the magnitude of the magnetisation in 50 kOe decreases as the Ca content decreases.  $M(H)$  shows hysteresis in all these compositions, most obviously in  $\text{Sr}_{0.25}\text{Ca}_{1.75}\text{CrSbO}_6$  for which we found a remanent magnetisation,  $M_r$ , of  $0.160 \mu_B \text{ f.u.}^{-1}$  and a coercive field,  $H_C$ , of 0.042 kOe, see Figure 12 and Table 11.

The ferromagnetic order was confirmed by neutron diffraction; additional Bragg scattering was visible in the 011 and 101 reflections of the compositions  $x = 1.0, 1.5$  and  $2.0$  below the magnetic ordering temperature. No weak peaks corresponding to the antiferromagnetic structure of  $\text{Sr}_2\text{CrSbO}_6$  were present in any of these diffraction patterns. In the case of  $\text{SrCaCrSbO}_6$  the structural model refined using the D2b data was applied to the D1b data and only the magnetic structure was refined, see Figure S8. For  $\text{Sr}_{0.5}\text{Ca}_{1.5}\text{CrSbO}_6$  and  $\text{Ca}_2\text{CrSbO}_6$  the structure refined from the SXRD data were used as a starting model. For  $\text{Ca}_2\text{CrSbO}_6$  and  $\text{Sr}_{0.5}\text{Ca}_{1.5}\text{CrSbO}_6$  the spins were found to be aligned in the  $xz$  plane, as shown in Figure 13. As  $a \sim b$  for  $\text{SrCaCrSbO}_6$ , the orientation of the spins could not be unambiguously determined so the spins were also constrained to be aligned in the  $xz$  plane. At 2 K the ordered moment,  $M_O$ , of Cr(III) was refined to be  $1.769(22) \mu_B$  in  $\text{SrCaCrSbO}_6$ ,  $2.460(15) \mu_B$  in  $\text{Sr}_{0.5}\text{Ca}_{1.5}\text{CrSbO}_6$  and  $2.56(3) \mu_B$  in  $\text{Ca}_2\text{CrSbO}_6$ . The refined ordered moment of the Cr(III) ion as a function of temperature for all compositions bar  $x=0.5$  is shown in Figure 5 and shows that the magnetic transition temperature increases from 7 K for  $\text{SrCaCrSbO}_6$  to 14 K for  $\text{Ca}_2\text{CrSbO}_6$ . As can be seen from Figure 5, the ordered moment of  $\text{SrCaCrSbO}_6$  at 2 K is lower than those of the other two ferromagnetic compositions because the magnetic transition is incomplete at that temperature. The ordered moment of  $\text{Ca}_2\text{CrSbO}_6$  is within error of the value of  $2.6(2) \mu_B^3$  reported for this compound in the literature; however we found the moment to be orientated in the  $xz$  plane rather than along  $[110]$ .

## Discussion

The results presented above show that, although the unit-cell volume decreases approximately linearly with increasing  $x$ ,  $\text{Sr}_{2-x}\text{Ca}_x\text{CrSbO}_6$  does not exist as a continuous solid solution for  $0 \leq x \leq 1$ , but that phase separation occurs when  $x \sim 0.5$ . The replacement of 12.5 % strontium by calcium, i.e.  $x=0.25$ , induces a change in space group from  $\bar{1}1$  to  $P2_1/n$  but this sample appears monophasic in x-ray and neutron diffraction experiments. However, increasing the overall calcium content to  $x=0.5$  causes the sample to disproportionate into  $\text{Sr}_{1.55}\text{Ca}_{0.45}\text{Cr}_{1.02}\text{Sb}_{0.98}\text{O}_6$  and  $\text{Sr}_{1.33}\text{Ca}_{0.67}\text{Cr}_{1.02}\text{Sb}_{0.98}\text{O}_6$ , presumably because the different

alkaline-earth cations impose incompatible structural requirements on the network of vertex-sharing octahedra. No evidence of biphasic behaviour was seen in compositions in the range  $0.75 \leq x \leq 2$ . We shall return to this point below when we discuss the magnetic properties of these materials; there appears to be a close correlation between the switch from antiferromagnetism to ferromagnetism and the disproportionation of the sample.

The changes in bond lengths observed across the series are largely as expected. The increase in calcium content causes a systematic reduction in the mean Sr/Ca–O bond length (or  $\langle A-O \rangle$ ). In the case of biphasic  $Sr_{1.5}Ca_{0.5}CrSbO_6$  the value of  $\langle A-O \rangle$  is consistent with the conclusion that the sample has phase separated into a Sr-rich phase and a Ca-rich phase. Both have mean Sr/Ca–O bond lengths at room temperature that lie in between those of the  $x=0.25$  and  $x=0.75$  samples, where  $\langle A-O \rangle = 2.779$  Å and 2.771 Å respectively, but the Sr-rich  $x=0.45$  phase has a slightly longer  $\langle A-O \rangle$  bond length of 2.775 Å compared to the Ca-rich  $x=0.67$  phase where  $\langle A-O \rangle = 2.772$  Å. Although small, this difference in the mean Sr/Ca–O bond length of the two phases is also observed at 25 K and 2 K.

$Cr^{3+}$  and  $Sb^{5+}$  have very similar ionic radii of 0.615 Å and 0.60 Å<sup>13</sup> so it is surprising that such a high degree of B site cation order is maintained across the entire series. However, the slight difference in the size of the cations is reflected in the  $\langle B-O \rangle$  bond lengths as for all compounds except  $x=1.75$  the predominantly Cr-containing  $2d$  site ( $2f$  for  $Sr_2CrSbO_6$ ) has a longer  $\langle B-O \rangle$  bond length than the  $2c$  site ( $2g$  for  $Sr_2CrSbO_6$ ), which contains mainly Sb. Interestingly, for  $x < 0.75$   $\langle B-O \rangle$  is substantially smaller than the ideal  $Cr^{3+}-O$  and  $Sb^{5+}-O$  bond lengths of 2.015 Å and 2.00 Å calculated using the Shannon-Prewitt ionic radii<sup>13</sup> but the mean bond length increases in the more Ca-rich samples, reaching 1.996 Å in  $Ca_2CrSbO_6$ . This is closer to the value predicted by the ionic model, which suggests that the covalency of the  $Cr^{3+}-O$  bonds decreases with increasing calcium content. The decrease in covalency, which coincides with the switch from antiferromagnetic to ferromagnetic order, can be attributed to the relatively high acidity of  $Ca^{2+}$  compared to  $Sr^{2+}$ ; the smaller A-site cation will compete more effectively for the electron density on the oxide ion, thus reducing the amount available for the  $B-O$  bonds. Density functional theory (DFT) calculations have also indicated that a difference in the degree of covalency in bonds involving the A-site cation and Cr in  $Sr_2CrSbO_6$  and  $Ca_2CrSbO_6$ , in combination with structural differences, might be responsible for the switch from antiferromagnetic to ferromagnetic behaviour<sup>14</sup>. The Cr 3d: O 2p hybridisation in  $Sr_2CrSbO_6$  has also been calculated to be stronger than in  $Ca_2CrSbO_6$  resulting in a lower magnetic moment on the Cr ion in  $Sr_2CrSbO_6$ <sup>15</sup>.

In agreement with Retuerto *et al*, our neutron diffraction data show that the magnetic properties of the compounds in this solid solution switch from antiferromagnetic to ferromagnetic on changing the diamagnetic A-site cation from Sr to Ca. The structural and magnetic properties of  $\text{Ca}_2\text{CrSbO}_6$  reported here affirm the previous study of that composition, with the exception of the orientation of the moment, but we find that  $\text{Sr}_2\text{CrSbO}_6$  crystallises in the space group  $\bar{1}$  rather than  $I2/m$  or  $P2_1/n$ . We note that  $\text{LaSr}_2\text{Cr}_2\text{SbO}_9$  (or  $\text{La}_{0.67}\text{Sr}_{1.33}\text{Cr}_{1.33}\text{Sb}_{0.67}\text{O}_6$ ) was also recently found to adopt this space group<sup>16</sup>. With this new structural model a value of  $2.39(1) \mu_B$  was obtained for the ordered Cr(III) moment in the antiferromagnetic phase, which is significantly larger than the value of  $1.64 \mu_B$  reported by Retuerto *et al* and closer to the value of  $2.56(3) \mu_B$  found in  $\text{Ca}_2\text{CrSbO}_6$ . By synthesising the solid solution  $\text{Sr}_{2-x}\text{Ca}_x\text{CrSbO}_6$  we have shown that the dominant magnetic interaction changes from antiferromagnetic to ferromagnetic close to  $x = 0.5$  and certainly in the range  $0.45 \leq x \leq 0.75$ . These are, respectively, the estimated composition of the Sr-rich phase in the nominal  $\text{Sr}_{1.5}\text{Ca}_{0.5}\text{CrSbO}_6$  sample, from which weak reflections corresponding to antiferromagnetic order were detected, and the least Ca-rich composition for which  $\chi(T)$  shows clear ferromagnetic behaviour.

However, there are a number of inconsistencies between the above account and our susceptibility data, suggesting that the former is an oversimplification. Firstly, in the case of  $x=0$  there is a minimum in  $\chi(T)$  at  $\sim 5.5$  K, 6.5 K below the Néel temperature. No impurities were detected in this sample and we therefore ascribe this behaviour to the presence of spins that remain paramagnetic down to 2 K. These are likely to be associated with the small number of  $\text{Cr}^{3+}$  cations that lie on the  $2c$  site. More importantly,  $\chi(T)$  of the sample  $x=0.25$  has no turning points, suggesting that the sample is paramagnetic throughout the measured temperature range. In contrast, the neutron diffraction data show clear evidence of a Néel point at 5 K. However, the ordered magnetic moment of  $1.79 \mu_B$  per  $\text{Cr}^{3+}$  is only 75 % of that determined when  $x=0$ , suggesting that 25 % of the spins are not ordered. It is clear that the replacement of strontium by calcium weakens the antiferromagnetic interactions in this system and eventually leads to the onset of ferromagnetism. We suggest that the structural changes caused by the introduction of as little as 12.5 % calcium causes some atomic moments to decouple from the antiferromagnetic structure. The decoupled cations, which dominate the susceptibility at low temperatures, are likely to lie in regions with a relatively calcium-rich local environment where the local structure deviates significantly from the average structure. The suggestion that the local structure is easily distorted by the

introduction of calcium is consistent with the occurrence of disproportionation when the nominal calcium content reaches 25 %. The susceptibility of that sample also shows no turning points although very weak magnetic Bragg peaks are observed in the neutron diffraction data collected at 2 K. We assigned these to the strontium-rich phase, the calcium content of which, 22.5 %, substantially reduces the number of  $\text{Cr}^{3+}$  cations that participate in the antiferromagnetic ordering. In this sample the low-temperature susceptibility is dominated by the decoupled cations in the strontium-rich phase and all the cations in the paramagnetic calcium-rich phase. It is possible that the latter phase orders ferromagnetically at a temperature below 2 K, which is outside the range of our magnetometer. However, although the compositions having  $x=0.75$  and 1.0 clearly order ferromagnetically the relatively-low values of their saturation magnetisation suggest that the presence of relatively-high strontium concentrations in the ferromagnetic phases perturbs the magnetic structure in much the same way that the presence of calcium perturbs the antiferromagnetic order in samples having  $x \leq 0.5$ . Compositions with  $x \geq 1.25$  do not contain a high enough concentration of strontium to inhibit ferromagnetic ordering

The replacement of  $\text{Sr}^{2+}$  by  $\text{Ca}^{2+}$  is not expected to change the sign of the magnetic exchange constant along the Cr–O–O–Cr superexchange pathway but the concomitant structural changes will modify the strength of the interaction. It is likely that as a consequence of the tilting and rotation of the  $\text{BO}_6$  octahedra with respect to each other, the degree of  $\pi$  orbital overlap is no longer sufficient for the  $\pi$ –mediated superexchange to occur. Instead, the exchange interaction occurs via potential exchange, resulting in ferromagnetic order. A 1:1 ordered double perovskite of space group  $\text{P2}_1/n$  can be described by the Glazer tilt system  $a^-a^-b^+$ <sup>17</sup>. In  $\text{Sr}_{2-x}\text{Ca}_x\text{CrSbO}_6$  the in-phase tilt is about [001] and there is an out-of-phase tilt of equal value about [100] and [010], which can be described as a tilt about [110]. The tilting angle can be estimated as  $\phi=(180-\psi)/2$  where  $\psi=\text{B-O-B}$ <sup>18</sup>. An estimate of the tilt angle about [001] can be made by averaging the tilt angles arising from the B-O-B bond angles that lie in the  $xy$  plane. Similarly, the tilt angle about [110] can be estimated by averaging the tilt angles arising from the B-O-B bond angles that lie about  $xz$  and  $yz$ . As shown in Figure 14, the tilt about [110] increases markedly over the composition range  $0.25 < x < 2.0$ , which would disrupt the  $\pi$  –mediated superexchange pathway as shown, and Figure 15 shows that the tilts about [110] and [001] are of similar magnitude to each other across the  $\text{Sr}_{2-x}\text{Ca}_x\text{CrSbO}_6$  series. The increase in tilting between  $x=0.25$  to  $x=2.0$  is also clearly visible from the increased peak splitting in the XRD patterns shown in Figure S9. In the critical region between  $x=0.45$  and

$x=0.75$ , where the magnetic properties switch from antiferromagnetic to ferromagnetic, the tilts about [110] and [001] are both  $\sim 8^\circ$  and both increase to  $\sim 14^\circ$  as  $x$  approaches 2.0. Ferromagnetic potential exchange becomes increasingly dominant as the  $\text{BO}_6$  octahedra become more tilted with the Weiss temperature,  $\theta_w$ , becoming increasingly positive and  $T_C$  increasing with  $x$ . The breakdown of the  $\pi$  –mediated superexchange pathway coincides with an increase in the mean  $2d\text{--O}$  bond length as the covalency of the  $\text{Cr--O}$  bond decreases. The decrease in covalency also coincides with an increase in the ordered moment deduced from the NPD data collected on D1b at 2 K and an increase in the saturation magnetisation of  $M(H)$  with  $x$ .

To the authors' knowledge, no other examples of ferromagnetic double perovskites exist where both A-site cations and the  $B'$  cation are diamagnetic. The magnetic behaviour of these  $\text{Cr}^{3+}$  compounds contrasts sharply with that of the  $\text{Fe}^{3+}$  analogues,  $\text{Ca}_2\text{FeSbO}_6$  and  $\text{Sr}_2\text{FeSbO}_6$ , which show a degree of cation ordering comparable to that found in  $\text{Sr}_{2-x}\text{Ca}_x\text{CrSbO}_6$  but, instead of undergoing a transition to a magnetically-ordered phase, adopt a spin-glass phase at  $\sim 25$  K. The absence of long-range magnetic order was ascribed to competition between different superexchange interactions, for example those between nearest-neighbour (NN) and next-nearest-neighbour (NNN) cations<sup>19, 20</sup>. The difference in behaviour between the  $\text{Cr}^{3+}$ - and  $\text{Fe}^{3+}$ -containing compositions is likely to be caused by a change in the relative strength of the  $\sigma$  and  $\pi$  superexchange interactions on moving from  $\text{Fe}^{3+}:3d^5$  to  $\text{Cr}^{3+}:3d^3$ . Given the high degree of B-site cation order across the  $\text{Sr}_{2-x}\text{Ca}_x\text{CrSbO}_6$  series, interactions along either  $\text{Cr--O--Sb--O--Cr}$  or  $\text{Cr--O--O--Cr}$  pathways are likely to be responsible for the observed long-range magnetic order. The Type I antiferromagnetic structure found in  $\text{Sr}_2\text{CrSbO}_6$  is stabilised when the latter interaction is antiferromagnetic and dominant and the former interaction is either ferromagnetic or negligibly small<sup>21</sup>. As a consequence of the  $t_{2g}^3$  electronic configuration of the cation, superexchange interactions involving  $\text{Cr}^{3+}$  are dominated by  $\pi$  superexchange and, consistent with the above criterion, interactions via the relatively-short  $\text{Cr--O--O--Cr}$  superexchange pathway, which utilise the O  $2p_\pi$  orbitals, are likely to be stronger than those along the  $\text{Cr--O--Sb--O--Cr}$  pathway which involve weak  $\text{Sb } 5d_\pi\text{--O } 2p_\pi$  interactions. The interactions along the longer pathway are likely to be stronger and competitive when, as in the case of  $\text{Ca}_2\text{FeSbO}_6$  and  $\text{Sr}_2\text{FeSbO}_6$ , the  $e_g$  orbitals of the magnetic cation are half-filled and  $\sigma$  superexchange is also significant. We note that the magnetic structure of  $\text{Sr}_2\text{CrSbO}_6$  is essentially the same as that of  $\text{Sr}_2\text{OsInO}_6$ <sup>22</sup>, another perovskite containing a 1:1 ordered arrangement of a  $d^3$  cation and a diamagnetic  $d^{10}$

cation, although changes in bond strength, the degree of structural distortion and the detailed electronic structure of the cation result in the  $5d^3$  system having a higher Néel temperature and an ordered moment of only  $1.77(6) \mu_B$  per  $Os^{5+}$  cation.

The  $d^5$  systems  $Sr_2Mn(II)Mo(VI)O_6$ ,  $Sr_2Mn(II)W(VI)O_6$  and  $Ca_2Mn(II)W(IV)O_6$  provide a further comparison as they all crystallise in the space group  $P2_1/n$ , have fully ordered B sites and diamagnetic cations on the A and B' sites. They adopt a similar, albeit not identical, antiferromagnetic structures to  $Sr_2CrSbO_6$  with  $m_{x1}=-m_{x2}$ ;  $m_y=m_{2y}$  and  $m_{z1}=-m_{z2}$  and order at  $T_N = 12$  K, 13 K and 16 K respectively<sup>23</sup>. The octahedra in  $Sr_2MnMoO_6$  and  $Sr_2MnWO_6$  have similar tilt angles to the compositions  $x=0.67$  and  $0.75$  with tilts about  $[001]$  of  $9^\circ$  and  $9.5^\circ$  and tilts about  $[110]$  of  $8.95^\circ$  and  $9.275^\circ$ , respectively, and so these compounds could be on the cusp of a transition to ferromagnetic ordering. However  $Ca_2MnWO_6$  is far more distorted than even  $Ca_2CrSbO_6$ , with tilt angles about  $[110]$  and  $[001]$  of  $15.8^\circ$  and  $16.2^\circ$ , and yet still orders antiferromagnetically.  $LaCaMnNbO_6$ , which adopts the same type I antiferromagnetic structure as  $Sr_2CrSbO_6$ , is also highly distorted with tilt angles similar to  $Ca_2MnWO_6$  but is antiferromagnetic with  $T_N=9$  K<sup>18</sup>. Given that  $Mn^{2+}$  has a  $t_{2g}^3e_g^2$  electronic configuration, it is likely that in these cases  $\sigma$ -mediated superexchange plays a role in preserving the antiferromagnetic order. Providing an explanation for the contrasting behaviour of the  $3d^5:Fe^{3+}$  compounds described above as spin glasses and these antiferromagnetic compounds containing  $3d^5:Mn^{2+}$  lies beyond the scope of this study, but the answer might lie in the different energies of the  $d^0$  valence shell of  $Nb^{5+}$  and  $W^{6+}$  and the  $d^{10}$  shell of  $Sb^{5+}$ . Finally, we note that  $Ca_2LaRuO_6$ , wherein the magnetic species,  $Ru^{5+}$ , has a  $t_{2g}^3$  electronic configuration, is also a Type I antiferromagnet despite the octahedra being highly tilted with respect to each other ( $\phi_{110}=17.2^\circ$ ;  $\phi_{001}=17.0^\circ$ )<sup>21</sup> and the fact that only  $\pi$  –mediated superexchange is possible in this system. Thus it is clear that the level of tilting of the octahedra alone does not govern the magnetic properties of a double perovskite.

## Conclusion

All compositions in the series  $Sr_{2-x}Ca_xCrSbO_6$  that were investigated in this study ( $x=0, 0.25, 0.50, 0.75, 1.0, 1.25, 1.50, 1.75, 2.0$ ) crystallise in the  $P2_1/n$  space group with the exception of  $Sr_2CrSbO_6$ , which crystallises in the space group  $\bar{1}1$ . The extent of the tilting and rotation of the  $BO_6$  octahedra increases as the Ca content increases. The magnetic ordering in  $Sr_{2-x}Ca_xCrSbO_6$  switches from antiferromagnetic to ferromagnetic in the composition range  $0.45 < x < 0.75$ , wherein two perovskite-like phases coexist. The tilt angle about both  $[110]$  and

[001] in this region is  $\sim 8^\circ$  at 300 K, and it increases to  $\sim 14^\circ$  in the Sr-free ferromagnetic composition. There is clearly a difference in the behaviour of  $d^3$  and  $d^5$  cations in comparable systems. However, the tilt angle and the electron configuration are not the only parameters that govern the magnetic properties of a double perovskite, as some  $d^3$  systems that are more distorted than  $\text{Ca}_2\text{CrSbO}_6$  do not order ferromagnetically.

## Acknowledgments

We are grateful to E. Suard for experimental assistance at ILL and to the EPSRC for financial support under grant EP/M018954/1. We also thank Diamond Light Source Ltd (EE13284) for the award of beamtime and Dr C Murray for support on I11.

## References

1. Kobayashi, K. I.; Kimura, T.; Sawada, H.; Terakura, K.; Tokura, Y., Room-temperature magnetoresistance in an oxide material with an ordered double-perovskite structure. *Nature* **1998**, 395, 677-680.
2. Lin, Y. Q.; Chen, X. M., Dielectric, Ferromagnetic Characteristics, and Room-Temperature Magnetodielectric Effects in Double Perovskite  $\text{La}_2\text{CoMnO}_6$  Ceramics. *Journal of the American Ceramic Society* **2011**, 94, 782-787.
3. Retuerto, M.; Garcia-Hernandez, M.; Martinez-Lope, M. J.; Fernandez-Diaz, M. T.; Attfield, J. P.; Alonso, J. A., Switching from ferro- to antiferromagnetism in  $\text{A}_2\text{CrSbO}_6$  (A = Ca, Sr) double perovskites: a neutron diffraction study. *Journal of Materials Chemistry* **2007**, 17, 3555-3561.
4. Faik, A.; Igartua, J. M.; Gateshki, M.; Cuello, G. J., Crystal structures and phase transitions of  $\text{Sr}_2\text{CrSbO}_6$ . *Journal of Solid State Chemistry* **2009**, 182, 1717-1725.
5. Rietveld, H. M., A profile refinement method for nuclear and magnetic structures. *Journal of Applied Crystallography* **1969**, 2, 65-71.
6. Larson, A. C.; Von Dreele, R. B., *Los Alamos Natl. Lab. Rep. LAUR* **1994**, 86-748.
7. Argonne National Laboratory Compute X-ray Absorption. <http://11bm.xray.aps.anl.gov/absorb/absorb.php>
8. David, W., Powder diffraction peak shapes. Parameterization of the pseudo-Voigt as a Voigt function. *Journal of Applied Crystallography* **1986**, 19, 63-64.
9. Glazer, A., Simple ways of determining perovskite structures. *Acta Crystallographica Section A* **1975**, 31, 756-762.
10. Tahir-Kheli, R. A.; Callen, H. B.; Jarrett, H., Magnetic ordering in cubic crystals with first and second neighbor exchange. *Journal of Physics and Chemistry of Solids* **1966**, 27, 23-32.
11. Groen, W. A.; IJdo, D. J. W., Distrontium diantimonate(V). A Rietveld refinement of neutron powder diffraction data. *Acta Crystallographica Section C* **1988**, 44, 782-784.
12. Monteiro, O. C.; Marques, R.; Carvalho, M. D., Photocatalytic studies of antimonate compounds prepared by a self-combustion route. *Materials Chemistry and Physics* **2010**, 119, 418-423.
13. Shannon, R., Revised effective ionic radii and systematic studies of interatomic distances in halides and chalcogenides. *Acta Crystallographica Section A* **1976**, 32, 751-767.

14. Baidya, S.; Saha-Dasgupta, T., Effect of **A** cation on magnetic properties of double perovskite compounds: From ferromagnetic  $\text{Ca}_2\text{CrSbO}_6$  to antiferromagnetic  $\text{Sr}_2\text{CrSbO}_6$ . *Physical Review B* **2012**, 86, 024440.
15. Dutta, A.; Sinha, T. P., Electronic structure of  $\text{A}_2\text{CrSbO}_6$  [A= Sr, Ca]: Ab-initio study. *Journal of Physics and Chemistry of Solids* **2013**, 74, 250-254.
16. Hunter, E. C.; Battle, P. D.; Paria Sena, R.; Hadermann, J., Ferrimagnetism as a consequence of cation ordering in the perovskite  $\text{LaSr}_2\text{Cr}_2\text{SbO}_9$ . *Journal of Solid State Chemistry* **2017**, 248, 96-103.
17. Woodward, P., Octahedral Tilting in Perovskites. I. Geometrical Considerations. *Acta Crystallographica Section B* **1997**, 53, 32-43.
18. Bos, J. W. G.; Attfield, J. P., Structural and Magnetic Properties of the Double Perovskite  $\text{LaCaMnNbO}_6$ . *Zeitschrift für anorganische und allgemeine Chemie* **2004**, 630, 2248-2252.
19. Battle, P. D.; Gibb, T. C.; Herod, A. J.; Hodges, J. P., Sol-gel synthesis of the magnetically frustrated oxides  $\text{Sr}_2\text{FeSbO}_6$  and  $\text{SrLaFeSnO}_6$ . *Journal of Materials Chemistry* **1995**, 5, 75-78.
20. Battle, P. D.; Gibb, T. C.; Herod, A. J.; Kim, S.-H.; Munns, P. H., Investigation of magnetic frustration in  $\text{A}_2\text{FeMO}_6$  (A = Ca, Sr, Ba; M = Nb, Ta, Sb) by magnetometry and Mossbauer spectroscopy. *Journal of Materials Chemistry* **1995**, 5, 865-870.
21. Battle, P. D.; Goodenough, J. B.; Price, R., The crystal structures and magnetic properties of  $\text{Ba}_2\text{LaRuO}_6$  and  $\text{Ca}_2\text{LaRuO}_6$ . *Journal of Solid State Chemistry* **1983**, 46, 234-244.
22. Paul, A. K.; Sarapulova, A.; Adler, P.; Reehuis, M.; Kanungo, S.; Mikhailova, D.; Schnelle, W.; Hu, Z.; Kuo, C.; Siruguri, V.; Rayaprol, S.; Soo, Y.; Yan, B.; Felser, C.; Hao Tjeng, L.; Jansen, M., Magnetically Frustrated Double Perovskites: Synthesis, Structural Properties, and Magnetic Order of  $\text{Sr}_2\text{BOsO}_6$  (B = Y, In, Sc). *Zeitschrift für anorganische und allgemeine Chemie* **2015**, 641, 197-205.
23. Muñoz, A.; Alonso, J. A.; Casais, M. T.; Martínez-Lope, M. J.; Fernández-Díaz, M. T., Crystal and magnetic structure of the complex oxides  $\text{Sr}_2\text{MnMoO}_6$ ,  $\text{Sr}_2\text{MnWO}_6$  and  $\text{Ca}_2\text{MnWO}_6$  : a neutron diffraction study. *Journal of Physics: Condensed Matter* **2002**, 14, 8817.
24. Momma, K.; Izumi, F., VESTA 3 for three-dimensional visualization of crystal, volumetric and morphology data. *Journal of Applied Crystallography* **2011**, 44, 1272-1276.



Table 1 – Structural parameters of Sr<sub>2</sub>CrSbO<sub>6</sub> at 300 K, 25 K and 2 K (Space Group  $I\bar{1}$ )

		300 K	25 K	2 K
$a/\text{\AA}$		5.55664(8)	5.54733(20)	5.53808(22)
$b/\text{\AA}$		5.57821(8)	5.54810(20)	5.53662(23)
$c/\text{\AA}$		7.84771(10)	7.87012(12)	7.89660(14)
$\alpha/^\circ$		89.9979(32)	90.2184(24)	90.1931(27)
$\beta/^\circ$		89.9668(24)	89.7533(24)	89.8548(30)
$\gamma/^\circ$		89.9374(11)	90.2271(7)	90.0665(13)
$V/\text{\AA}^3$		243.248(6)	242.214(13)	242.125(15)
Sr	$x$	0.4990(14)	0.4991(14)	0.4956(10)
$4i$	$y$	0.4991(4)	0.4987(11)	0.4964(11)
	$z$	0.2499(13)	0.2505(5)	0.2506(5)
	$U_{\text{iso}}/\text{\AA}^2$	0.00633(18)	0.00197(18)	0.00088(28)
	Occupancy	1	1	1
Cr/Sb1	$U_{\text{iso}}/\text{\AA}^2$	0.00097(23)	0	0
$2f(0\frac{1}{2}0)$	Cr Occupancy	0.979(1)	0.979(1)	0.979(1)
	Sb Occupancy	0.021(1)	0.021(1)	0.021(1)
Cr/Sb2	$U_{\text{iso}}/\text{\AA}^2$	0.00097(23)	0	0
$2g(\frac{1}{2}00)$	Cr Occupancy	0.021(1)	0.021(1)	0.021(1)
	Sb Occupancy	0.979(1)	0.979(1)	0.979(1)
O1	$x$	0.2451(13)	0.2273(9)	0.2204(13)
$4i$	$y$	0.24268(127)	0.2231(11)	0.2174(12)
	$z$	-0.0227(6)	-0.0061(10)	-0.00401(109)
	$U_{\text{iso}}/\text{\AA}^2$	0.0078(9)	0.00443(76)	0.0031(7)
	Occupancy	1	1	1
O2	$x$	0.2566(14)	0.2771(12)	0.2766(12)
$4i$	$y$	0.74572(153)	0.7258(11)	0.7203(10)
	$z$	0.0158(7)	0.0189(4)	0.01324(29)
	$U_{\text{iso}}/\text{\AA}^2$	0.0070(8)	0.00246(32)	0.0022(6)
	Occupancy	1	1	1
O3	$x$	0.4933(10)	0.5171(13)	0.5168(13)
$4i$	$y$	0.03808(35)	0.0249(15)	0.0087(14)
	$z$	0.2494(12)	0.2512(9)	0.24728(87)
	$U_{\text{iso}}/\text{\AA}^2$	0.0073(4)	0.00268(68)	0.0031(5)
	Occupancy	1	1	1

Table 2 – Bond lengths (Å) in Sr<sub>2</sub>CrSbO<sub>6</sub> at 300 K, 25 K and 2 K.

	300 K	25 K	2 K
Sr – O1	2.628(11)	2.610(9)	2.606(8)
Sr – O1	2.698(11)	2.669(10)	2.614(9)
Sr – O1	2.871(11)	2.892(11)	2.957(8)
Sr – O1	2.936(11)	2.945(9)	2.963(9)
Sr – O2	2.661(10)	2.5450(18)	2.560(3)
Sr – O2	2.724(12)	2.749(7)	2.710(6)
Sr – O2	2.837(12)	2.820(7)	2.860(5)
Sr – O2	2.898(10)	3.0335(18)	3.017(3)
Sr – O3	2.572(2)	2.631(10)	2.701(11)
Sr – O3	2.744(10)	2.687(10)	2.703(9)
Sr – O3	2.828(10)	2.866(10)	2.838(11)
Sr – O3	3.007(2)	2.921(9)	2.839(9)
<Sr – O>	2.784	2.781	2.781
Cr/Sb1 – O1	1.985(7)	1.991(7)	1.986(9)
Cr/Sb1 – O2	1.983(8)	1.985(8)	1.960(8)
Cr/Sb1 – O3	1.978(9)	1.966(7)	1.998(7)
<Cr/Sb1-O>	1.982	1.981	1.981
Cr/Sb2 – O1	1.967(7)	1.959(7)	1.963(9)
Cr/Sb2 – O2	1.965(8)	1.962(8)	1.984(8)
Cr/Sb2 – O3	1.969(9)	1.984(7)	1.956(7)
<Cr/Sb2 – O>	1.967	1.968	1.968

Table 3 – Bond angles (°) in  $\text{Sr}_2\text{CrSbO}_6$  at 300 K, 25 K and 2 K.

	300 K	25 K	2 K
O1 – Cr/Sb1 – O2	90.7(4)	90.17(16)	90.60(15)
O1 – Cr/Sb1 – O3	90.09(21)	90.3(4)	91.23(33)
O2 – Cr/Sb1 – O3	90.11(23)	90.33(17)	90.10(14)
<O – Cr/Sb1 – O>	90.30	90.27	90.64
O1 – Cr/Sb2 – O2	90.4(4)	90.37(18)	90.69(15)
O1 – Cr/Sb2 – O3	90.15(20)	91.3(4)	92.44(33)
O2 – Cr/Sb2 – O3	90.15(23)	90.46(18)	90.28(15)
<O – Cr/Sb2 – O>	90.23	90.71	91.14
Cr/Sb1–O1–Cr/Sb2	169.28(26)	168.38(25)	165.70(15)
Cr/Sb1–O2–Cr/Sb2	172.36(33)	165.36(8)	165.76(15)
Cr/Sb1–O3–Cr/Sb2	167.46(12)	170.28(28)	173.92(27)
<Cr/Sb1–O– Cr/Sb2>	169.70	168.01	168.46

Table 4 – Structural parameters of Sr-rich phase in nominal  $\text{Sr}_{1.5}\text{Ca}_{0.5}\text{CrSbO}_6$  at 300 K, 25 K and 2 K

		300 K	25 K	2 K
$a/\text{\AA}$		5.54989(8)	5.54234(9)	5.54250(9)
$b/\text{\AA}$		5.53228(10)	5.52521(11)	5.52551(11)
$c/\text{\AA}$		7.82205(16)	7.81300(17)	7.81237(18)
$\beta/^\circ$		90.022(6)	90.027(5)	90.019(6)
$V/\text{\AA}^3$		240.165(7)	239.255(8)	239.254(8)
Sr/Ca	$x$	0.0005(5)	-0.0010(5)	-0.0013(5)
$4e$	$y$	0.0085(6)	0.0132(5)	0.0120(6)
	$z$	0.2505(17)	0.2503(17)	0.2507(18)
	$U_{\text{iso}}/\text{\AA}^2$	0.00707(20)	0.00289(22)	0.00340(24)
	Ca Occupancy	0.225	0.225	0.225
	Sr Occupancy	0.775	0.775	0.775
Cr/Sb1	$U_{\text{iso}}/\text{\AA}^2$	0.00070(20)	0.00029(22)	0.00010(23)
$2d (\frac{1}{2} 0 0)$	Cr Occupancy	0.969(1)	0.969(1)	0.969(1)
	Sb Occupancy	0.031(1)	0.031(1)	0.031(1)
Cr/Sb2	$U_{\text{iso}}/\text{\AA}^2$	0.00070(20)	0.00029(22)	0.00010(23)
$2c (\frac{1}{2} 0 \frac{1}{2})$	Cr Occupancy	0.051(1)	0.051(1)	0.051(1)
	Sb Occupancy	0.949(1)	0.949(1)	0.949(1)
O1	$x$	0.0497(4)	0.0527(4)	0.0523(4)
$4e$	$y$	0.4965(7)	0.4954(6)	0.4960(7)
	$z$	0.2484(18)	0.2480(16)	0.2482 (20)
	$U_{\text{iso}}/\text{\AA}^2$	0.00773(15)	0.00452(15)	0.00449(16)
O2	$x$	0.7280(11)	0.7260(12)	0.7237(10)
$4e$	$y$	0.2716(14)	0.2750(14)	0.2754(14)
	$z$	0.0283(7)	0.0295(8)	0.0311(6)
	$U_{\text{iso}}/\text{\AA}^2$	0.00773(15)	0.00452(15)	0.00449(16)
O3	$x$	0.2334(11)	0.2298(12)	0.2323(10)
$4e$	$y$	0.2335(14)	0.2316(14)	0.2311(13)
	$z$	0.9786(7)	0.9764(8)	0.9773(6)
	$U_{\text{iso}}/\text{\AA}^2$	0.00773(15)	0.00452(15)	0.00449(16)

Table 5 – Structural parameters of Ca-rich phase in nominal  $\text{Sr}_{1.5}\text{Ca}_{0.5}\text{CrSbO}_6$  at 300 K, 25 K and 2 K

		300 K	25 K	2 K
$a/\text{\AA}$		5.53317(24)	5.52536(25)	5.52538(26)
$b/\text{\AA}$		5.52279(20)	5.51640(22)	5.51659(23)
$c/\text{\AA}$		7.80851(25)	7.79872(24)	7.79830(26)
$\beta/^\circ$		90.054(6)	90.052(6)	90.051(7)
$V/\text{\AA}^3$		238.616(15)	237.706(16)	237.702(17)
Sr/Ca	$x$	0.9979(13)	0.9970(13)	0.9982(13)
$4e$	$y$	0.0162(7)	0.0190(7)	0.0192(7)
	$z$	0.2525(18)	0.2534(15)	0.2525(19)
	$U_{\text{iso}}/\text{\AA}^2$	0.00707(20)	0.00289(22)	0.00340(24)
	Ca Occupancy	0.265	0.265	0.265
	Sr Occupancy	0.735	0.735	0.735
Cr/Sb1	$U_{\text{iso}}/\text{\AA}^2$	0.00070(20)	0.00029(22)	0.00010(23)
$2d (\frac{1}{2} 0 0)$	Cr Occupancy	0.957(1)	0.957(1)	0.957(1)
	Sb Occupancy	0.043(1)	0.043(1)	0.043(1)
Cr/Sb2	$U_{\text{iso}}/\text{\AA}^2$	0.00070(20)	0.00029(22)	0.00010(23)
$2c (\frac{1}{2} 0 \frac{1}{2})$	Cr Occupancy	0.063(1)	0.063(1)	0.063(1)
	Sb Occupancy	0.937(1)	0.937(1)	0.937(1)
O1	$x$	0.0574(10)	0.0587(10)	0.0576(10)
$4e$	$y$	0.4928(9)	0.4911(9)	0.4910(10)
	$z$	0.2491(18)	0.2482(19)	0.2487(21)
	$U_{\text{iso}}/\text{\AA}^2$	0.00773(15)	0.00452(15)	0.00449(16)
O2	$x$	0.7247(22)	0.7237(23)	0.7244(28)
$4e$	$y$	0.2782(23)	0.2789(25)	0.2784(30)
	$z$	0.0293(17)	0.0318(17)	0.0295(16)
	$U_{\text{iso}}/\text{\AA}^2$	0.00773(15)	0.00452(15)	0.00449(16))
O3	$x$	0.2256(23)	0.2236(25)	0.2236(28)
$4e$	$y$	0.2274(23)	0.2253(26)	0.2254(31)
	$z$	0.9733(17)	0.9713(17)	0.9689(16)
	$U_{\text{iso}}/\text{\AA}^2$	0.00773(15)	0.00452(15)	0.00449(16)

Table 6 Bond lengths (Å) for each perovskite phase in nominal  $\text{Sr}_{1.5}\text{Ca}_{0.5}\text{CrSbO}_6$  at 300 K, 25 K and 2 K

	300 K		25 K		2 K	
Phase	Sr-rich	Ca-rich	Sr-rich	Ca-rich	Sr-rich	Ca-rich
Sr/Ca – O1	2.497(3)	2.464(8)	2.487(3)	2.460(8)	2.490(4)	2.460(9)
Sr/Ca – O1	2.713(6)	2.653(6)	2.681(5)	2.627(6)	2.691(5)	2.624(6)
Sr/Ca – O1	2.846(6)	2.909(6)	2.876(5)	2.932(6)	2.867(5)	2.932(6)
Sr/Ca – O1	3.055(3)	3.075(8)	3.059(4)	3.075(8)	3.055(4)	3.074(9)
Sr/Ca – O2	2.515(12)	2.48(2)	2.500(12)	2.46(2)	2.477(12)	2.484(19)
Sr/Ca – O2	2.724(11)	2.722(16)	2.712(11)	2.706(16)	2.717(10)	2.712(17)
Sr/Ca – O2	2.792(11)	2.744(17)	2.776(13)	2.742(16)	2.780(12)	2.733(18)
Sr/Ca – O2	3.071(11)	3.138(19)	3.105(11)	3.168(18)	3.121(11)	3.144(19)
Sr/Ca – O3	2.586(10)	2.539(16)	2.564(10)	2.524(16)	2.572(10)	2.510(16)
Sr/Ca – O3	2.724(11)	2.693(17)	2.709(12)	2.676(17)	2.707(10)	2.672(18)
Sr/Ca – O3	2.783(12)	2.776(18)	2.770(13)	2.777(17)	2.776(12)	2.78(2)
Sr/Ca – O3	2.997(11)	3.076(17)	3.039(11)	3.100(17)	3.024(11)	3.115(16)
<Sr/Ca – O>	2.775	2.772	2.773	2.771	2.773	2.770
Cr/Sb1 – O1	1.987(14)	1.985(14)	1.991(13)	1.991(15)	1.988(16)	1.986(17)
Cr/Sb1 – O2	1.977(7)	1.990(11)	1.982(7)	1.989(12)	1.978(7)	1.987(15)
Cr/Sb1 – O3	1.971(7)	1.981(12)	1.978(7)	1.982(13)	1.966(7)	1.984(15)
<Cr/Sb1-O>	1.978	1.985	1.984	1.987	1.977	1.986
Cr/Sb2 – O1	1.963(14)	1.971(14)	1.959(13)	1.963(15)	1.961(16)	1.966(16)
Cr/Sb2 – O2	1.981(6)	1.968(11)	1.963(7)	1.970(12)	1.986(7)	1.967(15)
Cr/Sb2 – O3	1.970(7)	1.967(12)	1.976(7)	1.968(13)	1.974(7)	1.970(15)
<Cr/Sb2 – O>	1.971	1.969	1.966	1.967	1.974	1.968

Table 7 – Bond angles (°) for each perovskite phase of nominal composition  $\text{Sr}_{1.5}\text{Ca}_{0.5}\text{CrSbO}_6$  at 300 K, 25 K and 2 K

	300 K		25 K		2 K	
Phase	Sr-rich	Ca-rich	Sr-rich	Ca-rich	Sr-rich	Ca-rich
O1 – Cr/Sb1 – O2	90.82(21)	90.1(4)	90.71(22)	90.1(4)	91.22(19)	90.3(4)
O1 – Cr/Sb1 – O3	90.80(20)	90.4(4)	90.63(21)	90.0(4)	90.80(28)	90.7(4)
O2 – Cr/Sb1 – O3	90.5(4)	90.1(7)	90.4(4)	90.4(8)	90.90(35)	90.6(10)
<O – Cr/Sb1 – O>	90.71	90.2	90.58	90.17	90.97	90.53
O1 – Cr/Sb2 – O2	90.58(18)	90.2(4)	90.54(19)	90.7(4)	90.81(17)	90.4(4)
O1 – Cr/Sb2 – O3	90.88(17)	90.7(4)	90.76(19)	90.6(4)	90.91(16)	90.1(4)
O2 – Cr/Sb2 – O3	91.9(4)	91.6(8)	92.0(4)	91.4(8)	92.5(4)	91.3(10)
<O – Cr/Sb2 – O>	91.12	90.83	91.10	90.9	91.41	90.60
Cr/Sb1–O1–Cr/Sb2	163.89(11)	161.39(30)	162.94(12)	160.89(31)	163.06(12)	161.25(33)
Cr/Sb1–O2–Cr/Sb2	163.75(33)	162.0(8)	162.6(4)	160.9(8)	161.64(27)	161.8(9)
Cr/Sb1–O3–Cr/Sb2	167.66(30)	163.8(7)	166.12(33)	162.5(8)	166.72(25)	161.8(8)
<Cr/Sb1–O– Cr/Sb2>	165.10	162.40	163.89	161.43	163.8	161.62

Table 8 – Structural parameters of SrCaCrSbO<sub>6</sub> at 300 K, 25 K and 2 K (Space Group P2<sub>1</sub>/n)

		300 K	25 K	2 K
$a/\text{\AA}$		5.50868(8)	5.49997(14)	5.49859(16)
$b/\text{\AA}$		5.50863(7)	5.50393(14)	5.50294(17)
$c/\text{\AA}$		7.78357(6)	7.77122(16)	7.76938(18)
$\beta/^\circ$		89.9649(17)	89.939(4)	89.944(5)
$V/\text{\AA}^3$		236.194(5)	235.246(10)	235.089(11)
Sr/Ca	$x$	-0.0015(5)	-0.0039(8)	-0.0038(9)
$4e$	$y$	0.02036(8)	0.02284(34)	0.0234(4)
	$z$	0.2496(8)	0.2502(14)	0.2505(17)
	$U_{\text{iso}}/\text{\AA}^2$	0.00937(6)	0.00522(28)	0.00540(32)
Cr/Sb1	$U_{\text{iso}}/\text{\AA}^2$	0.001578(22)	0.00029(21)	0.00107(28)
$2d\ (\frac{1}{2}\ 0\ 0)$	Cr Occupancy	0.957(1)	0.957(1)	0.957(1)
	Sb Occupancy	0.043(1)	0.043(1)	0.043(1)
Cr/Sb2	$U_{\text{iso}}/\text{\AA}^2$	0.001578(22)	0.00029(21)	0.00107(28)
$2c\ (\frac{1}{2}\ 0\ \frac{1}{2})$	Cr Occupancy	0.083(1)	0.083(1)	0.083(1)
	Sb Occupancy	0.907(1)	0.907(1)	0.907(1)
O1	$x$	0.0611(4)	0.0614(5)	0.0606(6)
$4e$	$y$	0.49088(32)	0.4891(4)	0.4887(5)
	$z$	0.2480(6)	0.2470(9)	0.2475(11)
	$U_{\text{iso}}/\text{\AA}^2$	0.00818(31)	0.0058(4)	0.0065(5)
O2	$x$	0.7155(6)	0.7152(10)	0.7161(11)
$4e$	$y$	0.28518(57)	0.2849(10)	0.2856(12)
	$z$	0.0360(8)	0.0369(5)	0.0375(6)
	$U_{\text{iso}}/\text{\AA}^2$	0.00591(73)	0.0034(11)	0.0040(13)
O3	$x$	0.2248(6)	0.2218(9)	0.2222(11)
$4e$	$y$	0.22338(70)	0.2203(12)	0.2194(15)
	$z$	0.9735(4)	0.9699(5)	0.9700(6)
	$U_{\text{iso}}/\text{\AA}^2$	0.00877(76)	0.0067(12)	0.0018(13)



Table 9 – Bond lengths (Å) in SrCaCrSbO<sub>6</sub> at 300 K, 25 K and 2 K.

	300 K	25 K	2 K
Sr/Ca – O1	2.432(5)	2.441(5)	2.445(6)
Sr/Ca – O1	2.6147(9)	2.591(3)	2.585(3)
Sr/Ca – O1	2.9370(18)	2.960(3)	2.964(3)
Sr/Ca – O1	3.087(3)	3.072(5)	3.067(6)
Sr/Ca – O2	2.419(5)	2.408(8)	2.405(10)
Sr/Ca – O2	2.707(5)	2.687(8)	2.682(9)
Sr/Ca – O2	2.748(6)	2.746(9)	2.747(11)
Sr/Ca – O2	3.202(5)	3.219(8)	3.224(9)
Sr/Ca – O3	2.517(5)	2.481(9)	2.483(10)
Sr/Ca – O3	2.702(5)	2.680(7)	2.679(9)
Sr/Ca – O3	2.724(6)	2.732(8)	2.730(10)
Sr/Ca – O3	3.106(5)	3.149(9)	3.150(10)
<Sr/Ca – O>	2.766	2.764	2.763
Cr/Sb1 – O1	1.990(5)	1.996(7)	1.990(9)
Cr/Sb1 – O2	1.989(3)	1.985(5)	1.992(6)
Cr/Sb1 – O3	1.963(4)	1.967(6)	1.961(7)
<Cr/Sb1-O>	1.981	1.983	1.981
Cr/Sb2 – O1	1.960(5)	1.950(7)	1.953(9)
Cr/Sb2 – O2	1.984(3)	1.984(5)	1.978(6)
Cr/Sb2 – O3	1.974(4)	1.978(6)	1.982(8)
<Cr/Sb2 – O>	1.973	1.971	1.971

Table 10 – Bond angles (°) in SrCaCrSbO<sub>6</sub> at 300 K, 25 K and 2 K.

	300 K	25 K	2 K
O1 – Cr/Sb1 – O2	91.06(10)	91.05(15)	91.16(17)
O1 – Cr/Sb1 – O3	90.62(11)	90.29(15)	90.39(17)
O2 – Cr/Sb1 – O3	91.11(20)	90.33(34)	90.2(4)
<O – Cr/Sb1 – O>	90.93	90.56	90.64
O1 – Cr/Sb2 – O2	91.06(12)	91.33(17)	91.65(19)
O1 – Cr/Sb2 – O3	91.43(11)	90.85(16)	90.84(18)
O2 – Cr/Sb2 – O3	92.86(20)	92.26(33)	92.2(4)
<O – Cr/Sb2 – O>	91.78	91.48	91.56
Cr/Sb1–O1–Cr/Sb2	160.17(12)	159.98(17)	160.21(20)
Cr/Sb1–O2–Cr/Sb2	157.34(13)	157.08(23)	156.91(27)
Cr/Sb1–O3–Cr/Sb2	163.15(16)	161.04(26)	161.00(32)
<Cr/Sb1–O– Cr/Sb2>	160.22	159.37	159.37

Table 11 – Magnetic parameters of compounds in the series Sr<sub>2-x</sub>Ca<sub>x</sub>CrSbO<sub>6</sub>.

$x$	$\theta_W/K$	$\mu_{\text{eff}}/\mu_B$	$T_N/T_C /K$	$H_C/kOe$	$M_r/\mu_B$ per f.u. <sup>-1</sup>	$M_s/\mu_B$ per f.u. <sup>-1</sup>	$M_O/\mu_B$
0	-12.23(15)	3.705(6)	12				2.39(1)
0.25	-7.17(19)	3.841(8)	5				1.79(3)
0.50	-0.4(3)	3.657(12)	2				0.76(5)
0.75	5.38(72)	3.730(27)	3.5	0.042	0.116	2.21	
1.00	8.62(37)	3.731(18)	6.5	0.020	0.071	2.21	1.769(22)
1.25	11.82(22)	3.752(9)	9	0.033	0.126	2.50	
1.50	13.95(24)	3.632(9)	11	0.037	0.140	2.59	2.460(15)
1.75	15.54(29)	3.771(11)	12	0.042	0.160	2.64	
2.00	15.53(36)	3.933(29)	14	0.039	0.138	2.60	2.56(3)

## Figure captions

**Figure 1a** - Observed (red crosses) and calculated (green line) neutron powder diffraction profiles of  $\text{Sr}_2\text{CrSbO}_6$  at 300 K. Data were collected on D2b and fitted using the space group  $I\bar{1}$ . Reflection markers for  $\text{Sr}_2\text{CrSbO}_6$  are shown in black.

**Figure 1b** - Observed (red crosses) and calculated (green line) neutron powder diffraction profiles of  $\text{Sr}_2\text{CrSbO}_6$  at 2 K. Data were collected on D2b and fitted using the space group  $I\bar{1}$ . Reflection markers are shown for structural  $\text{Sr}_2\text{CrSbO}_6$  (black) and magnetic  $\text{Sr}_2\text{CrSbO}_6$  (red).

**Figure 2** – The ZFC and FC molar dc susceptibility and (inset) inverse susceptibility of  $\text{Sr}_2\text{CrSbO}_6$  measured in 100 Oe as a function of temperature.

**Figure 3** - Observed (red crosses) and calculated (green line) neutron powder diffraction profiles of  $\text{Sr}_2\text{CrSbO}_6$  at 2 K. Data were collected on D1b and fitted using the space group  $I\bar{1}$ . Reflection markers are shown for structural  $\text{Sr}_2\text{CrSbO}_6$  (black) and magnetic  $\text{Sr}_2\text{CrSbO}_6$  (red).

**Figure 4** – The nuclear and Type I magnetic structure of  $\text{Sr}_2\text{CrSbO}_6$  at 2 K<sup>24</sup>. Green and yellow octahedra represent the  $\text{CrO}_6$  and  $\text{SbO}_6$  octahedra, respectively. The Sr cations are represented by blue circles. The vectors associated with the Type I magnetic phase are represented by red arrows.

**Figure 5** – Cr(III) ordered moment derived from the neutron diffraction data as a function of temperature and composition. The dashed line is an estimate of the background level.

**Figure 6** - Observed (red crosses) and calculated (green line) neutron powder diffraction profiles in the range  $100 \leq 2\theta / ^\circ \leq 140$  of nominal  $\text{Sr}_{1.5}\text{Ca}_{0.5}\text{CrSbO}_6$  collected at room temperature on D2b. The profiles are fitted with a) one perovskite phase of space group  $P\bar{1}$ , b) a two-phase model where one phase is of the space group  $P2_1/n$  and the other is of the space group  $I\bar{1}$  and c) a two-phase model where both phases are of the space group  $P2_1/n$ . Reflection markers are shown a)  $\text{Sr}_{0.61}\text{Ca}_{1.39}\text{Sb}_2\text{O}_7$  (red) and  $P\bar{1}$   $\text{Sr}_{1.5}\text{Ca}_{0.5}\text{CrSbO}_6$  (black), b)  $\text{Sr}_{0.61}\text{Ca}_{1.39}\text{Sb}_2\text{O}_7$  (blue),  $P2_1/n$   $\text{Sr}_{1.33}\text{Ca}_{0.67}\text{Cr}_{1.02}\text{Sb}_{0.98}\text{O}_6$  (red) and  $I\bar{1}$   $\text{Sr}_{1.55}\text{Ca}_{0.45}\text{Cr}_{1.02}\text{Sb}_{0.98}\text{O}_6$  (black) and c) for  $\text{Sr}_{0.61}\text{Ca}_{1.39}\text{Sb}_2\text{O}_7$  (blue),  $P2_1/n$   $\text{Sr}_{1.33}\text{Ca}_{0.67}\text{Cr}_{1.02}\text{Sb}_{0.98}\text{O}_6$  (red) and  $P2_1/n$   $\text{Sr}_{1.55}\text{Ca}_{0.45}\text{Cr}_{1.02}\text{Sb}_{0.98}\text{O}_6$  (black).

**Figure 7** – The ZFC and FC molar dc susceptibility and (inset) inverse susceptibility of a)  $\text{Sr}_{1.75}\text{Ca}_{0.25}\text{CrSbO}_6$  and b)  $\text{Sr}_{1.5}\text{Ca}_{0.5}\text{CrSbO}_6$  measured in 100 Oe as a function of temperature.

**Figure 8** – Overlaid neutron powder diffraction profiles of a)  $\text{Sr}_{1.75}\text{Ca}_{0.25}\text{CrSbO}_6$  collected at 2 K (blue), 3 K (green), 4 K (orange) and 5 K (red) and b) nominal  $\text{Sr}_{1.5}\text{Ca}_{0.5}\text{CrSbO}_6$  collected at 2 K (blue) and 7 K (red) on D1b to illustrate the onset and growth of the magnetic Bragg peaks.

**Figure 9** – Variation of the  $a$ ,  $b$  and  $c$  lattice parameters and the volume of the unit cell of  $\text{Sr}_{2-x}\text{Ca}_x\text{CrSbO}_6$  at room temperature as a function of  $x$ . The grey shaded area signifies where the compound phase separates into  $\text{Sr}_{1.55}\text{Ca}_{0.45}\text{Cr}_{1.02}\text{Sb}_{0.98}\text{O}_6$  and  $\text{Sr}_{1.33}\text{Ca}_{0.67}\text{Cr}_{1.02}\text{Sb}_{0.98}\text{O}_6$  and the hashed line indicates where the space group of the perovskite changes from  $I\bar{1}$  to  $P2_1/n$ .

**Figure 10** – The ZFC (open triangle) and FC (open square) molar dc susceptibility of  $\text{Sr}_{2-x}\text{Ca}_x\text{CrSbO}_6$  for  $x=0.75$  (purple), 1.00 (blue), 1.25 (green), 1.50 (gold), 1.75 (orange) and 2.00 (red) measured in 100 Oe as a function of temperature.

**Figure 11** – Variation of the Weiss temperature,  $\theta$ , of  $\text{Sr}_{2-x}\text{Ca}_x\text{CrSbO}_6$  as a function of  $x$ .

**Figure 12** – The magnetisation per formula unit of  $\text{Sr}_{2-x}\text{Ca}_x\text{CrSbO}_6$  for  $x=0.75$  (purple), 1.00 (blue), 1.25 (green), 1.50 (gold), 1.75 (orange) and 2.00 (red) as a function of magnetic field at 2.5 K. Inset: The magnetisation per formula unit of  $\text{Sr}_{0.25}\text{Ca}_{1.75}\text{CrSbO}_6$  at 2.5 K in the range  $-0.75 \leq \mu_0 H \leq 0.75$ .

**Figure 13** – The nuclear and magnetic structure of  $\text{Ca}_2\text{CrSbO}_6$  at 2 K<sup>24</sup>. Green and yellow octahedra represent the  $\text{CrO}_6$  and  $\text{SbO}_6$  octahedra, respectively. The Ca cations are represented by blue circles. The vectors associated with the ferromagnetic phase are represented by red arrows.

**Figure 14** – A comparison of the crystal structures of the  $x=0.25$  and  $x=2.0$  compounds along 110 to demonstrate the breakdown of the  $J_2$   $\pi$ -mediated superexchange pathway on increasing the tilting angle about 110. Green and yellow octahedra represent the  $\text{BO}_6$  and  $\text{B}'\text{O}_6$  octahedra, respectively<sup>24</sup>.

**Figure 15** – Variation of the tilting angle,  $\phi$ , of  $\text{Sr}_{2-x}\text{Ca}_x\text{CrSbO}_6$  about 110 (red squares) and 001 (blue triangles) as a function of  $x$ . The grey shaded area signifies where the compound phase separates into  $\text{Sr}_{1.55}\text{Ca}_{0.45}\text{Cr}_{1.02}\text{Sb}_{0.98}\text{O}_6$  and  $\text{Sr}_{1.33}\text{Ca}_{0.67}\text{Cr}_{1.02}\text{Sb}_{0.98}\text{O}_6$ .

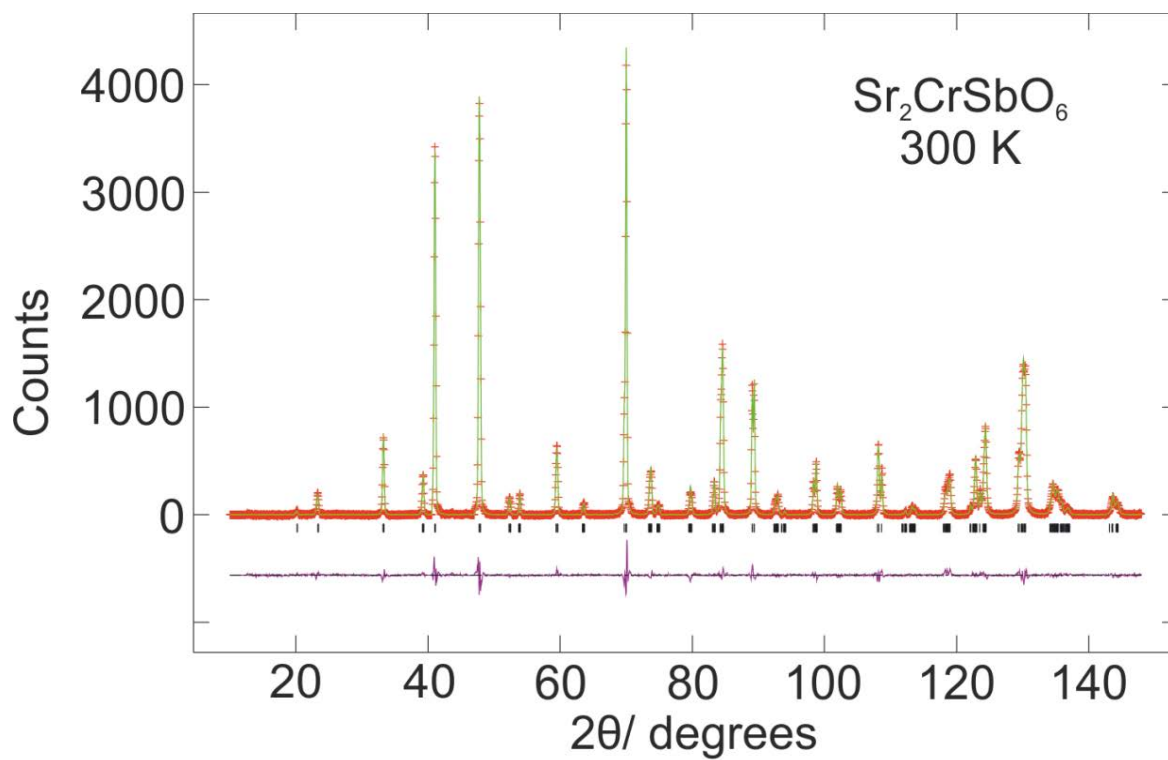


Figure 1a

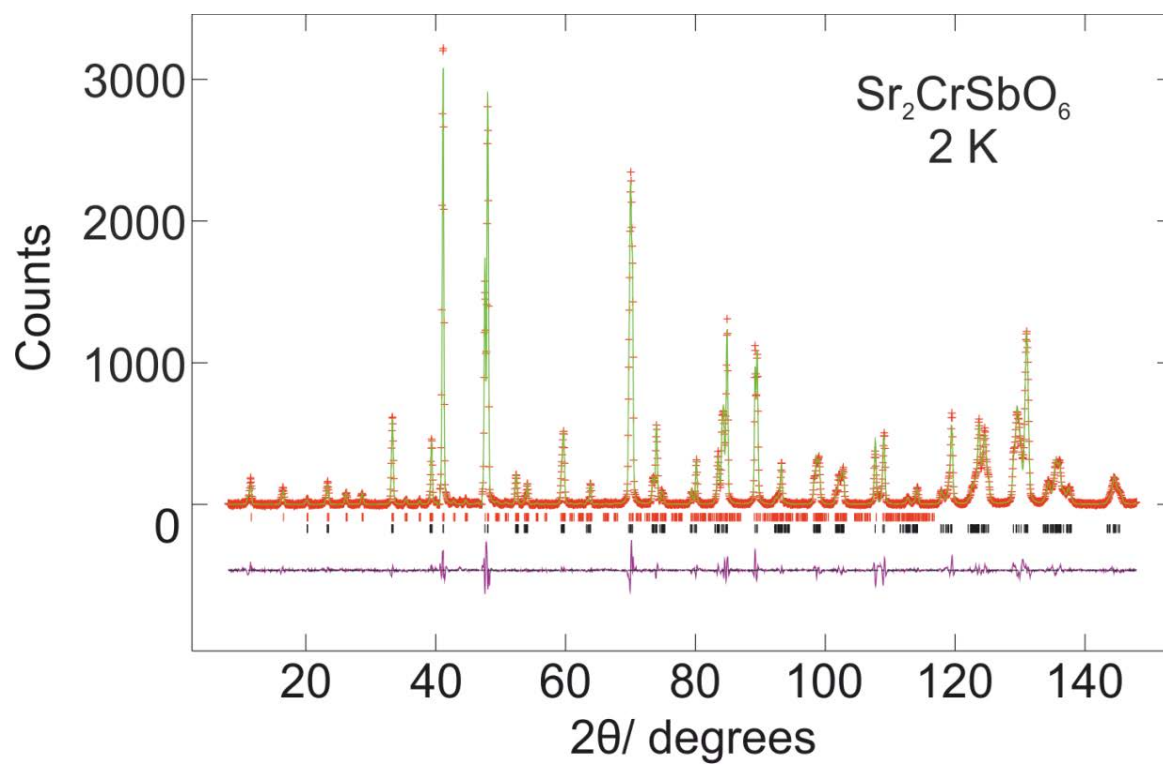


Figure 1b

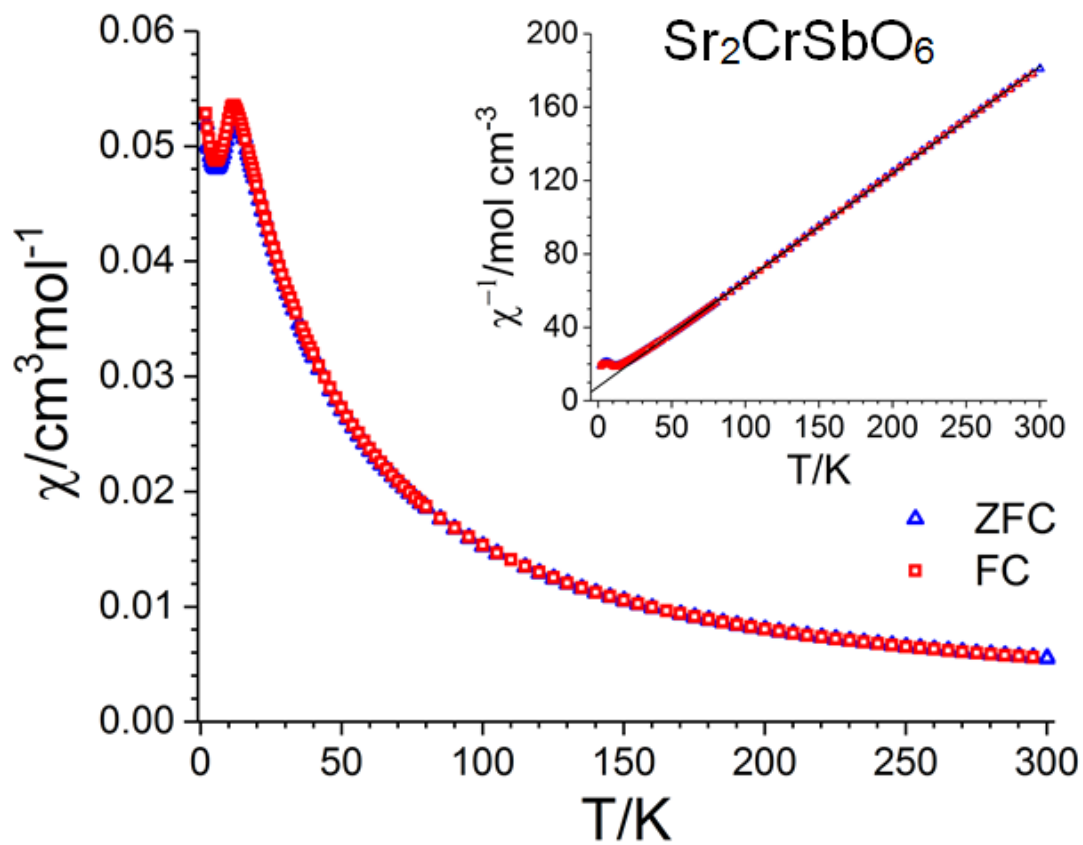


Figure 2

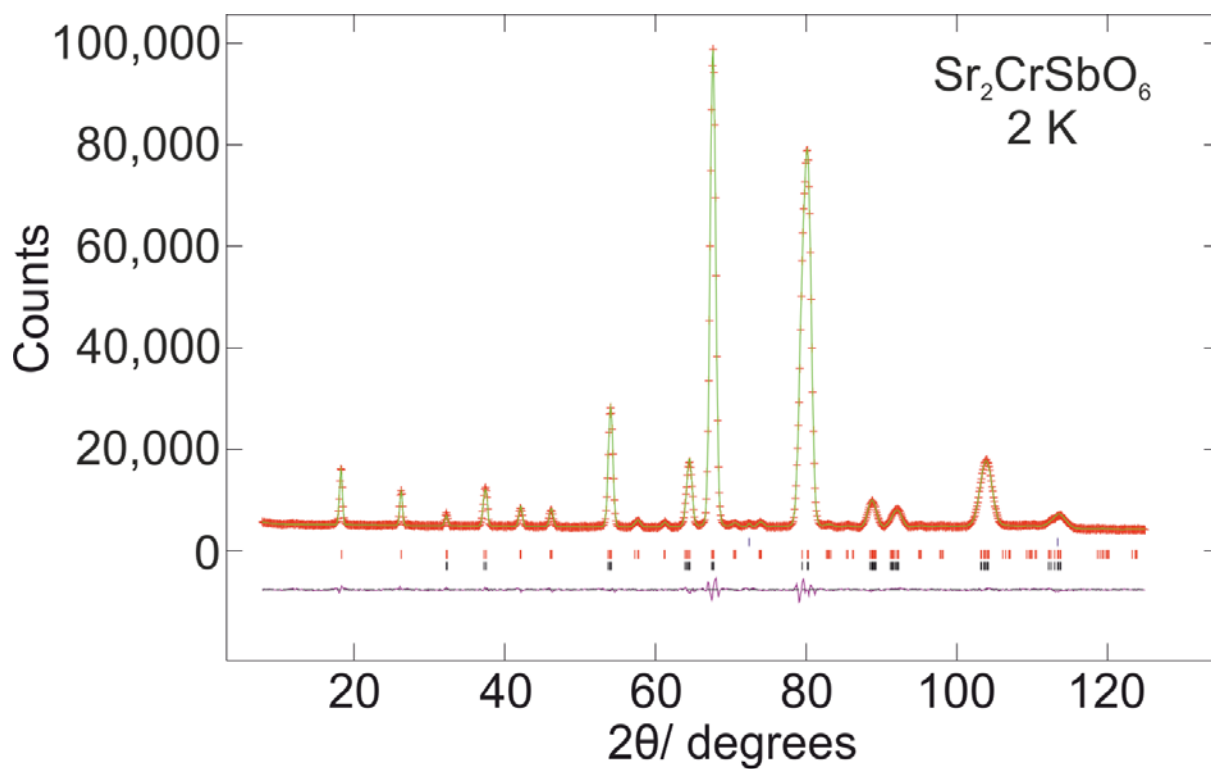


Figure 3

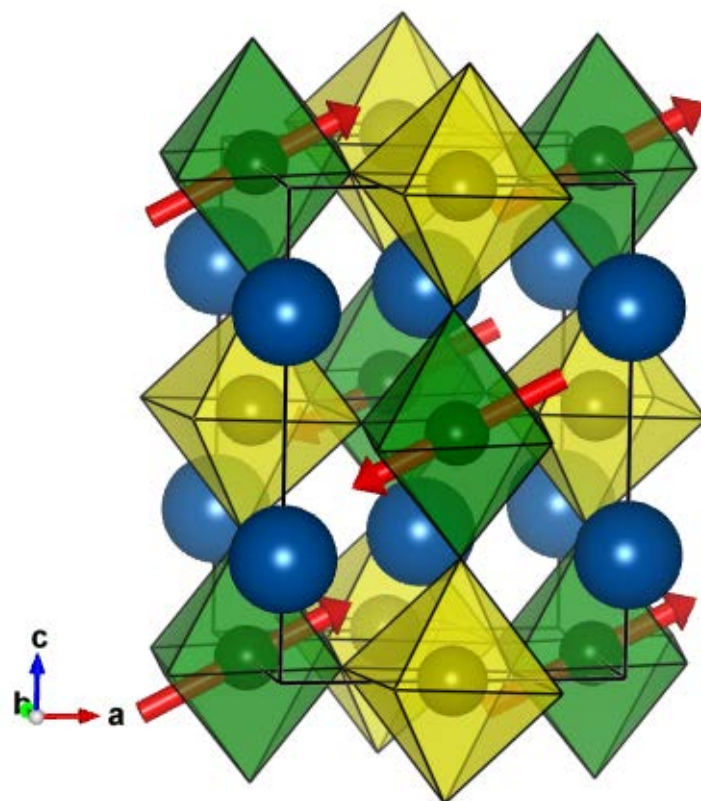


Figure 4

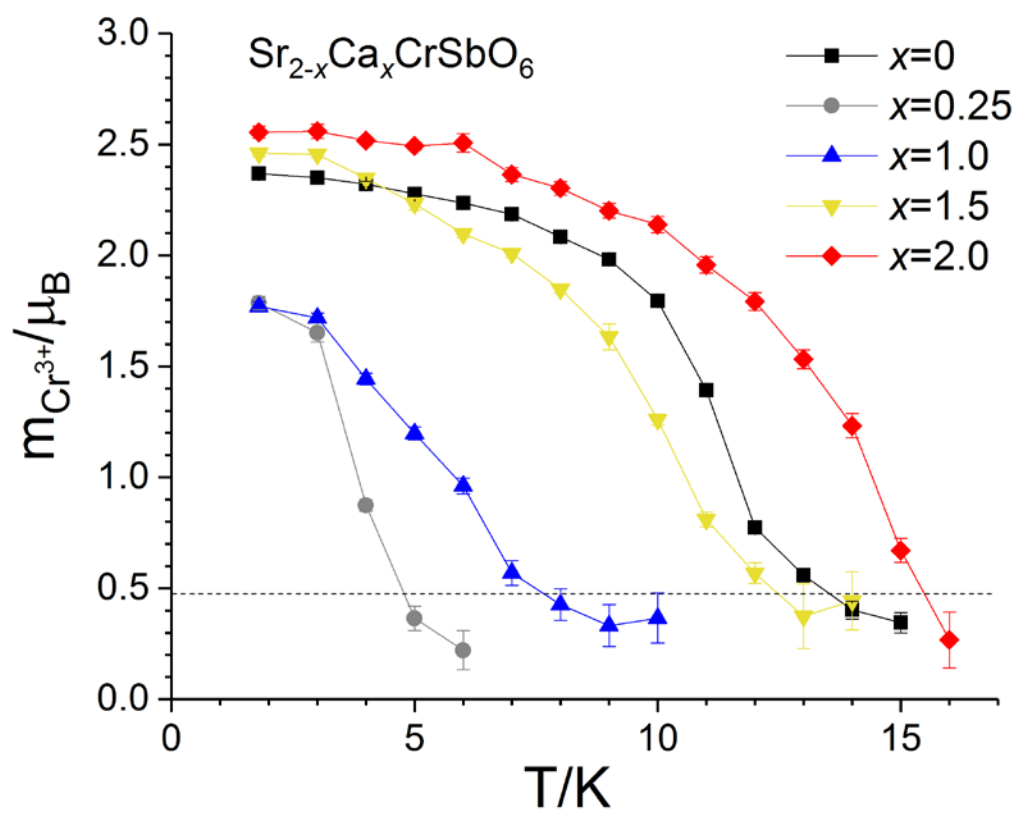
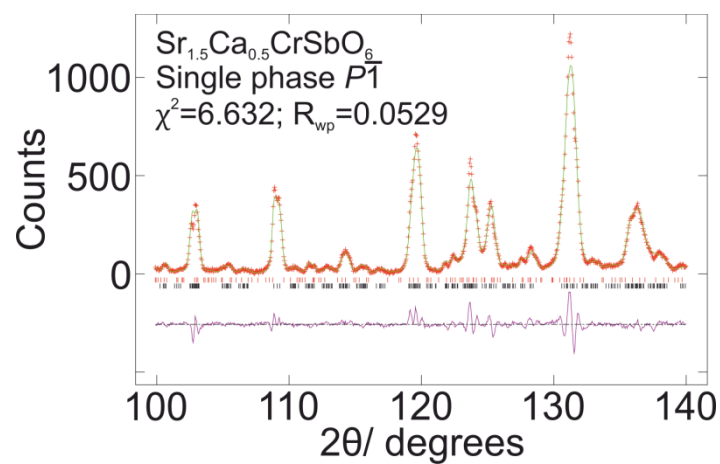
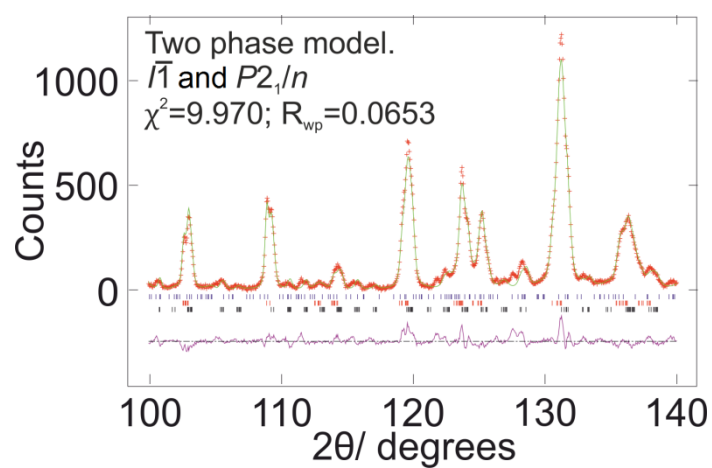


Figure 5

a)



b)



c)

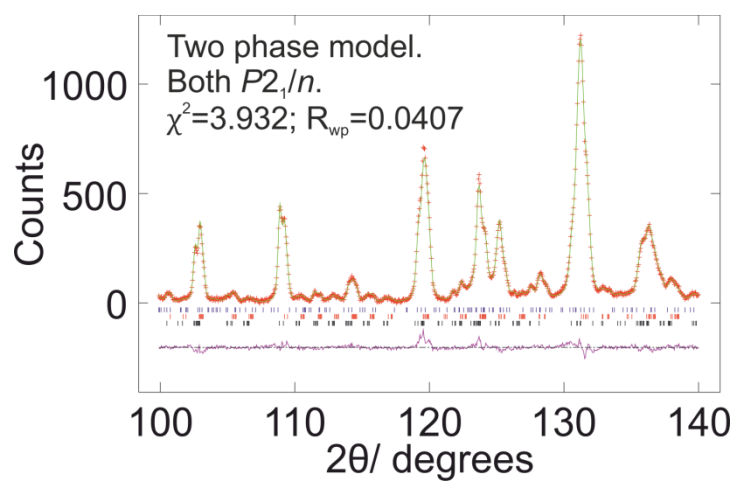
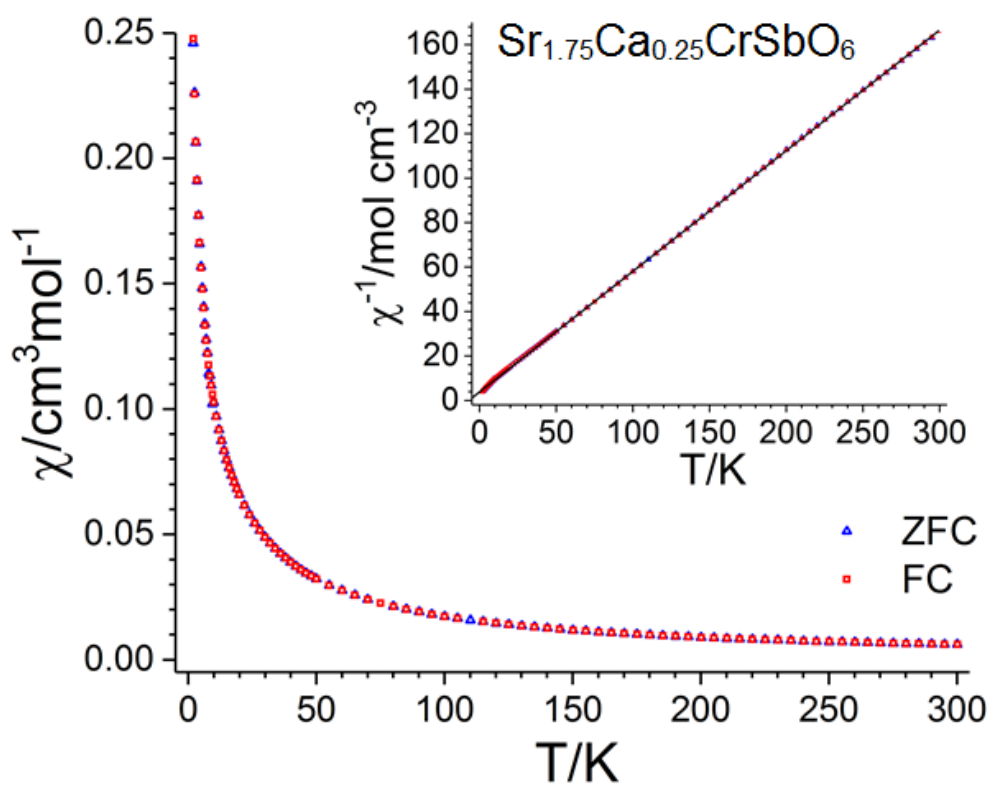


Figure 6



a)



b)

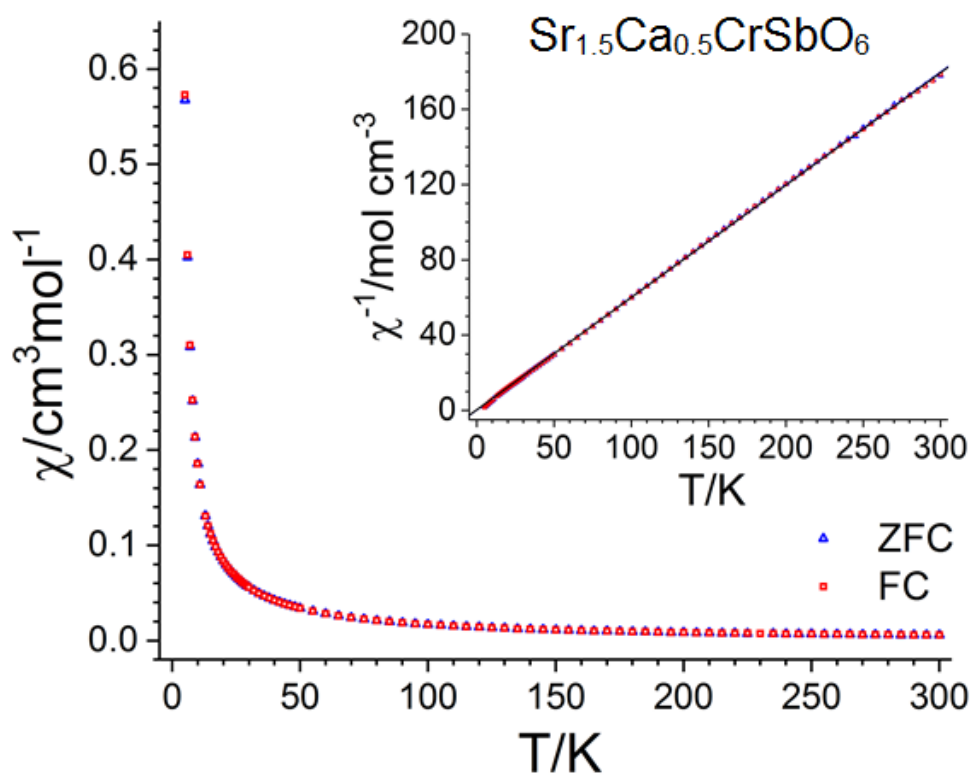
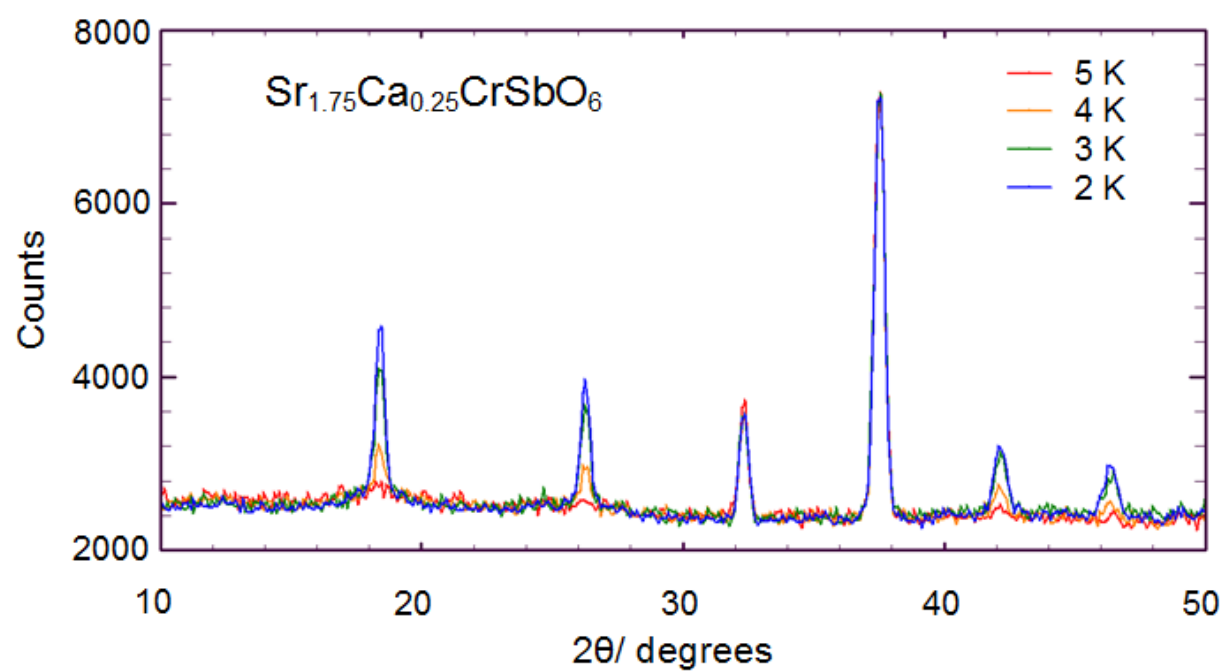


Figure 7

a)



b)

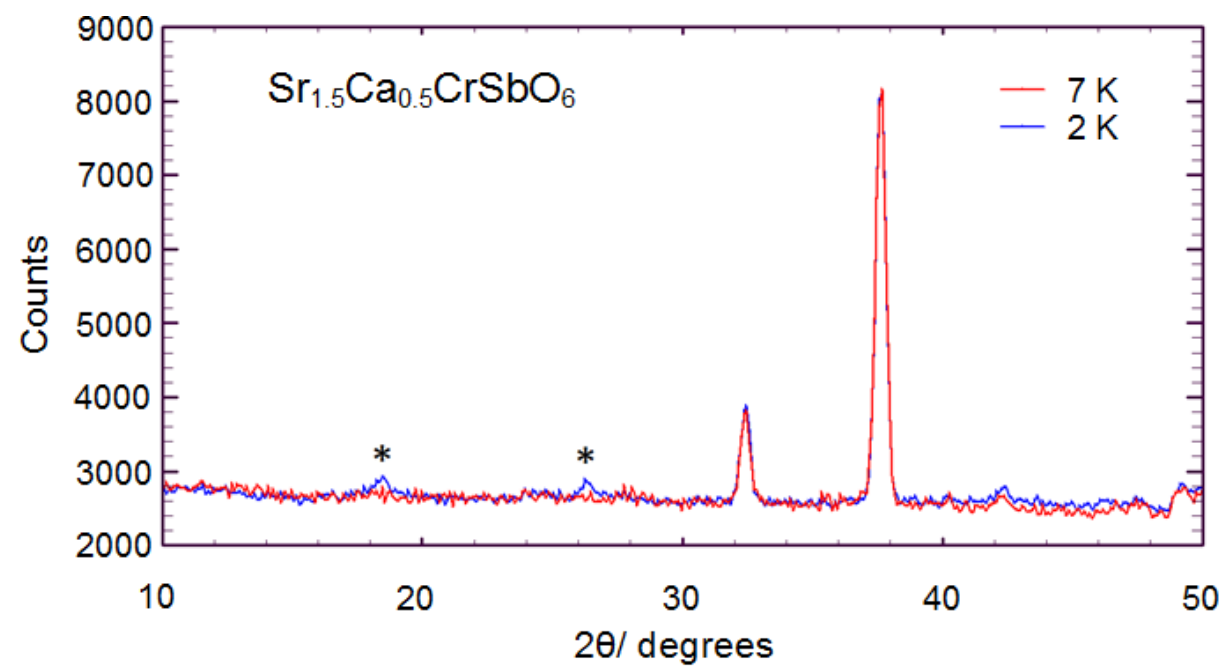


Figure 8

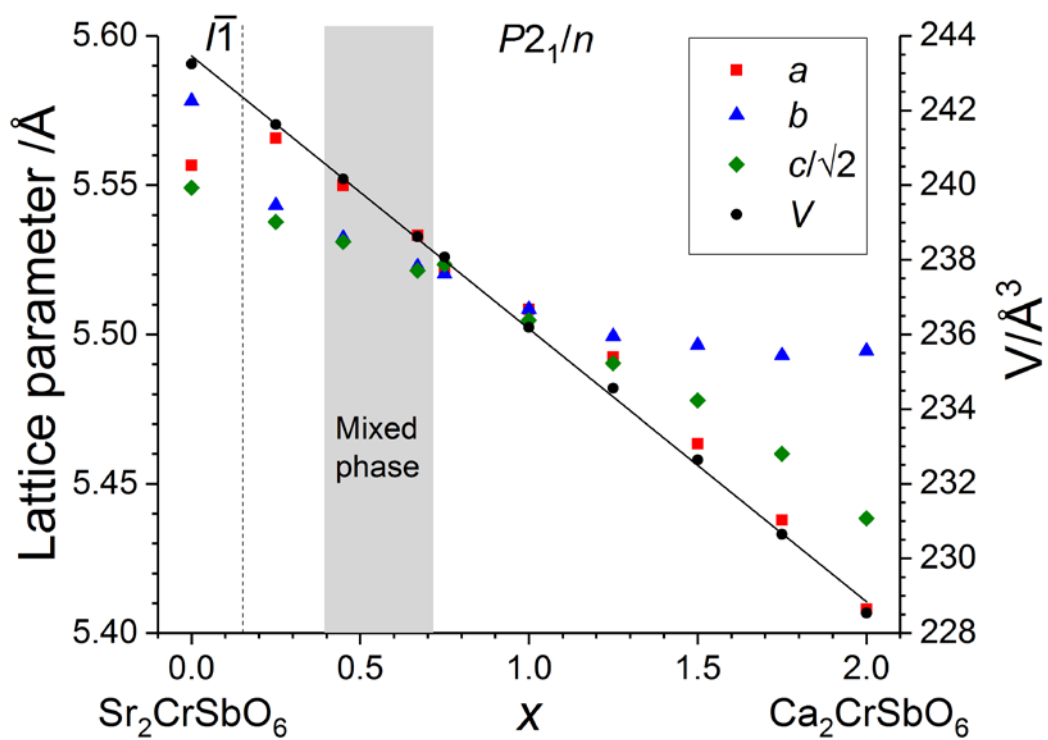


Figure 9

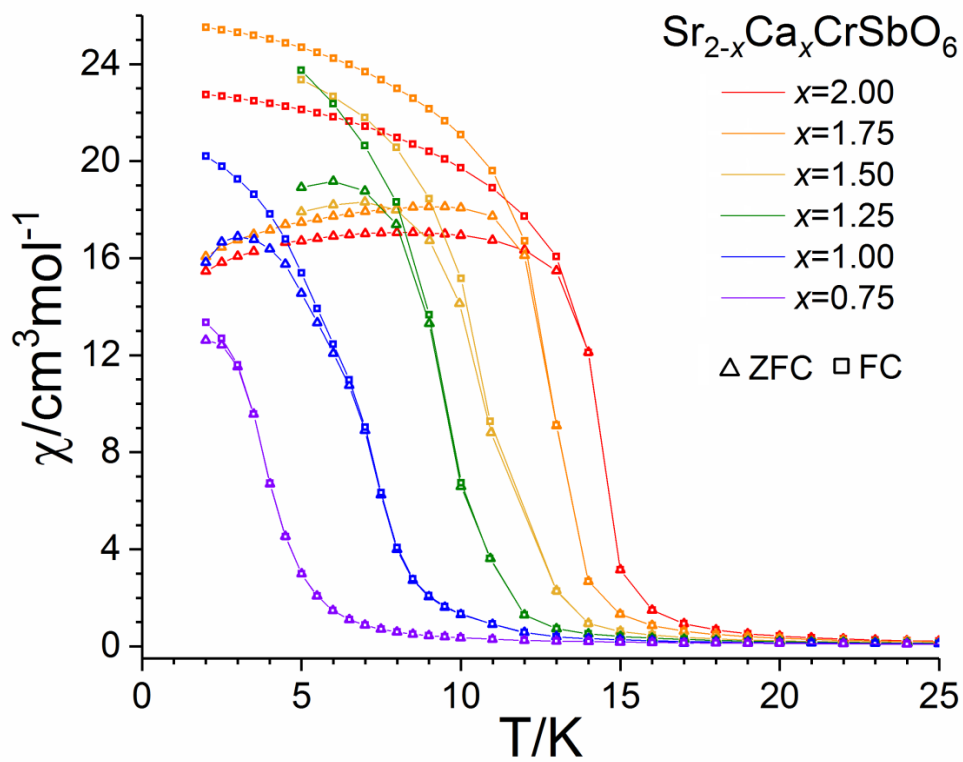


Figure 10

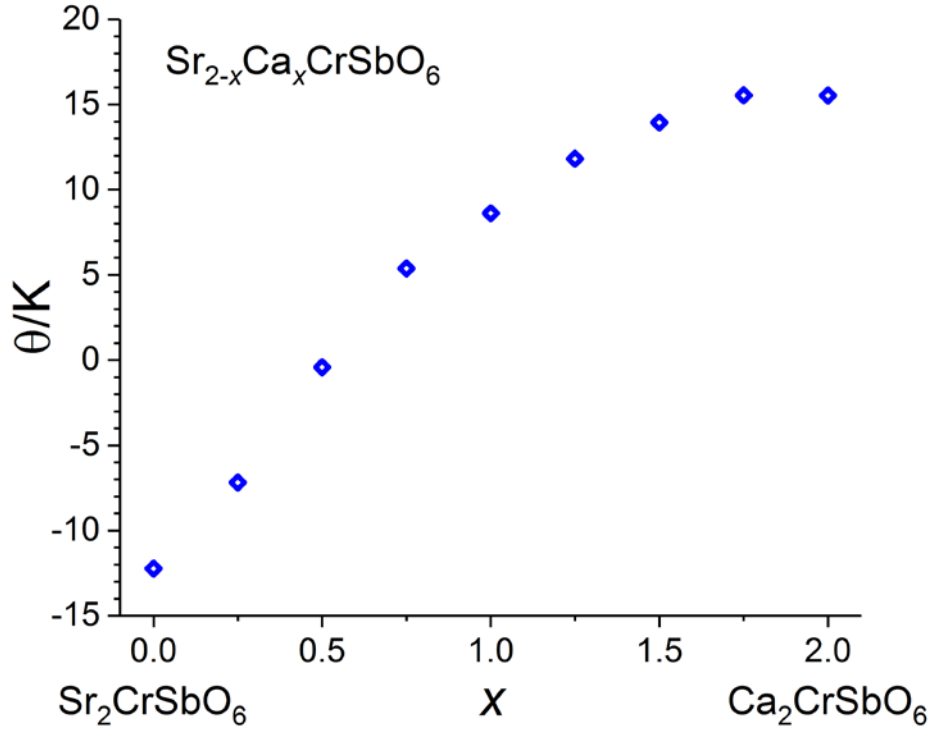


Figure 11

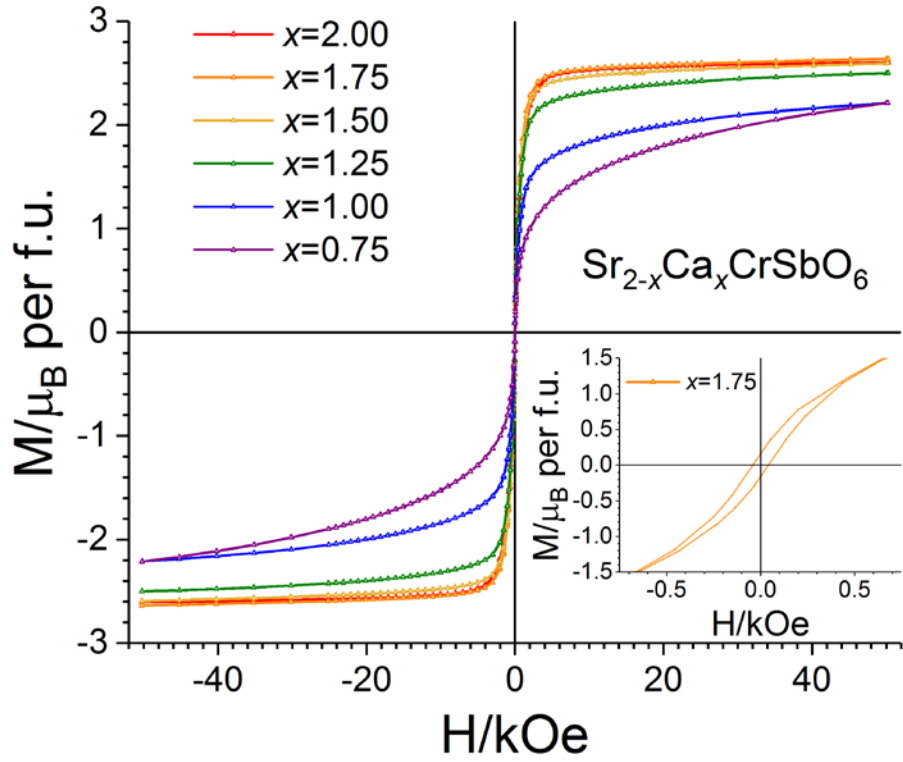


Figure 12

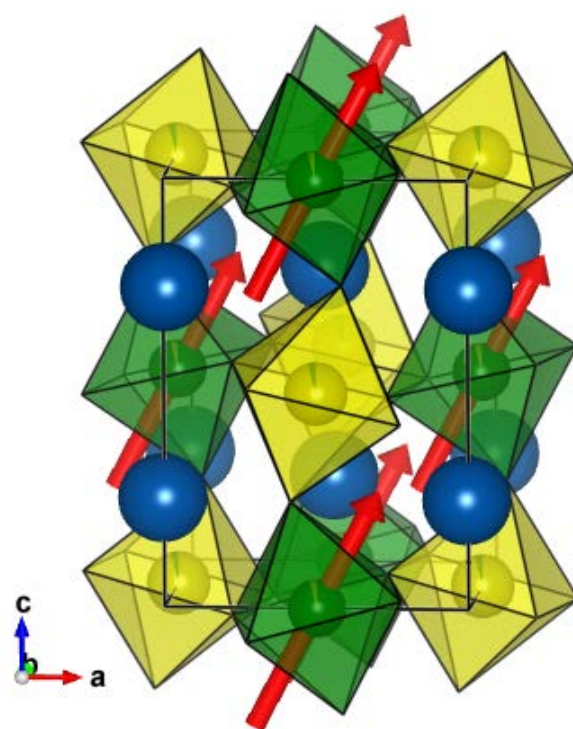


Figure 13

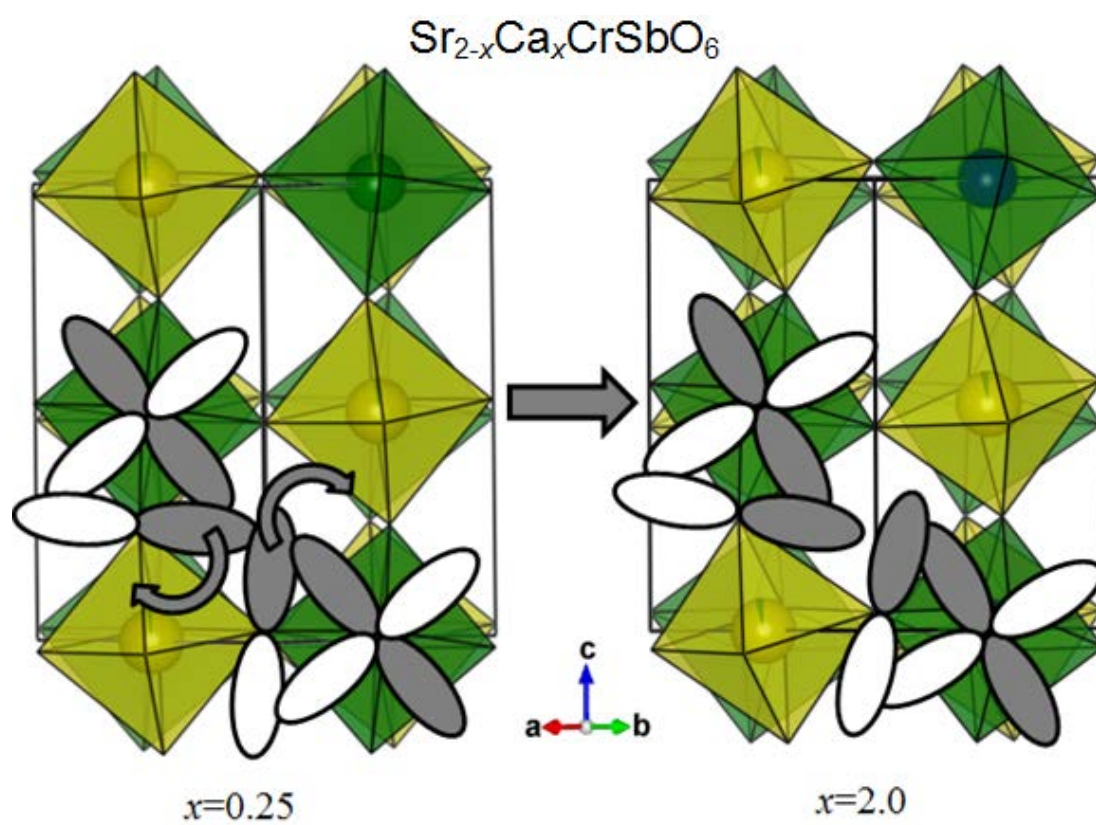


Figure 14

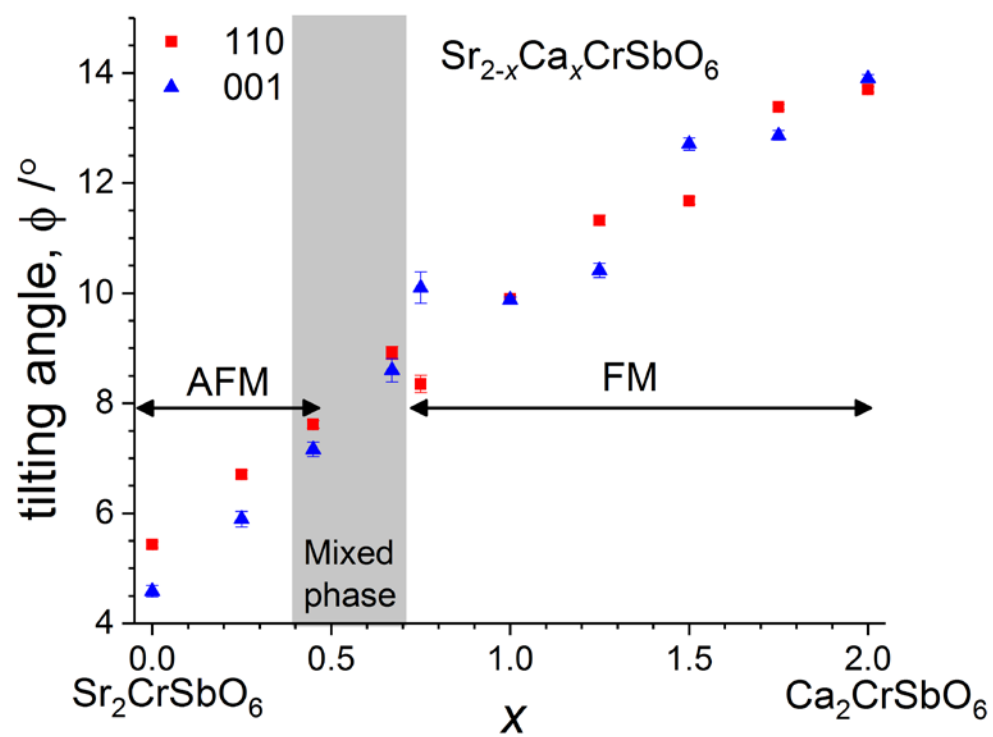


Figure 15